


## Numerical study of mass transfer and desorption behaviors in deformable porous media using a coupling lattice Boltzmann model

Qiang Ma<sup>1,2</sup>, Lijuan Zhao,<sup>1</sup> Huaneng Su,<sup>1</sup> Zhenqian Chen,<sup>3,\*</sup> and Qian Xu<sup>1,†</sup>

<sup>1</sup>*Institute for Energy Research, School of Energy and Power Engineering, Jiangsu University, 301 Xuefu Road, Zhenjiang 212013, People's Republic of China*

<sup>2</sup>*School of New Energy Vehicles, Nanchang Institute of Science and Technology, 998 Gezaoshan Road, Nanchang 330108, People's Republic of China*

<sup>3</sup>*Jiangsu Provincial Key Laboratory of Solar Energy Science and Technology, School of Energy and Environment, Southeast University, Nanjing 210096, People's Republic of China*

 (Received 23 February 2020; revised 29 June 2020; accepted 4 August 2020; published 24 August 2020)

The aim of this paper is to investigate the pore-scale mass transfer and desorption behaviors in deformable porous media using a coupling immersed boundary method (IBM)–lattice Boltzmann (LB) scheme. In this numerical model, a three-dimensional multiple-relaxation-time LB model is used to simulate fluid flow in porous media consisting of movable rigid adsorbent particles. To consider the effect of dynamic deformation of a porous structure, an improved immersed boundary method scheme is introduced to describe the fluid-structure interaction at the interface between the carrier gas and moving adsorbent particles. Moreover, a LB model for the convection diffusion equation is adopted to consider the mass transfer of adsorbate into the macropores and micropores of the porous adsorbent. This coupled IBM-LB model is used to illustrate the mass transfer and desorption processes in shrinkage deformation of the porous structure caused by the movement of rigid adsorbent particles along different directions. At the initial time, these adsorbent particles have a saturation adsorption amount, and the adsorbate in the macropores has the uniform concentration distribution. The numerical results show that the time history curve of the adsorbate concentration in the macropores can be divided into an upturn period and a downturn period during the dynamic desorption process. In the concentration upturn period governed by Langmuir adsorption kinetics, the shrinkage deformation of the porous structure along different directions has no remarkable effect on the mass transfer and desorption behaviors. However, during the concentration downturn period governed by the mass transfer rate of the adsorbate, the shrinkage deformation of the porous structure obviously decreases the efficiency of the desorption process. In addition, the roles of the deformation direction and morphology of the porous media in the desorption process are illustrated in this work.

DOI: [10.1103/PhysRevE.102.023309](https://doi.org/10.1103/PhysRevE.102.023309)

### I. INTRODUCTION

The process of mass transfer coupling with adsorption or desorption in deformable porous media is a widespread phenomenon in the natural environment and engineering fields, e.g., in the drying of porous media with shrinkage behavior, preparation of organized porous materials, contaminant transport processes in deformable soil, and swelling and shrinkage of coalbed methane reservoirs during gas adsorption and desorption [1–5]. The fluid flow, transfer, and ad- and desorption processes can induce the deformation of porous media [6,7]. In turn, the changing pore structure has a great influence on the characteristics of the momentum, heat, and mass transfer and ad and desorption processes due to variations in permeability, tortuosity, surface stress, and specific surface area. Therefore, suitable modeling and simulations are required to understand this complex influence mechanism [8].

The existing theoretical and numerical methods for studying transfer behaviors in deformable porous media are primarily based on the macroscopic or representative element volume scale model, such as homogenization and mixture theory [9–14]. Under the framework of the mixture theory model, Albro *et al.* [15] investigated solute transport, uptake, and desorption in soft biological porous tissues subjected to dynamic mechanical loading. The results showed that dynamic loading of deformable porous media can enhance the transport of solutes, as attributed to momentum exchange between the solute and solid matrix. Moreover, Yang [16] presented a mixed element method for describing gas flow and mass transfer coupling adsorption in deformable coalbed methane reservoirs, and the effects of deformation on permeability were considered in this model. Recently, Zhang [17] established a macroscopic theory model for deformable porous media interacting with the adsorption of fluid species. This comprehensive model derived from mixture theory can predict the coupled influences between the stretch-dependent adsorption and finite-strain deformation of porous materials, e.g., swelling or shrinkage of coal during CO<sub>2</sub> pressurization. One advantage of these macroscopic models is the feasibility

\*zqchen@seu.edu.cn

†xuqian@ujs.edu.cn

of comparison with experimental data, and the numerical results can be directly applied to optimize the transfer process of deformable porous media. However, as a typical multiscale process [18], it still lacks a suitable computational tool with which to investigate the kinetics of gas adsorption and desorption covering the micro-, meso-, and macroscales [19].

With respect to the microscale model for deformable porous media, the current literature mainly focuses on the sorption behaviors of adsorbate molecules on the surface of flexible adsorbent materials using molecular simulation, resulting in the structural transformation of adsorbent materials by changing the potential energy of interaction between the adsorbate and adsorbent [20–22]. Although molecular simulation has become an insightful method for clarifying the molecular-level mechanisms of adsorption-induced deformation, it is difficult to model the momentum, heat, and mass transfer processes coupled with ad- and desorption in the changing pore structures due to the computational resource limitations [19].

Compared to micro- and macroscale simulation, the lattice Boltzmann (LB) model, as an accurate and efficient mesoscale approach [23–27], has a potential advantage in elaborating the momentum, heat, and mass transfer in porous media, especially at the pore scale [28–30]. To date, the LB model has been applied to investigate the flow and heat and mass transfers in deformable porous media. With respect to pore-scale studies of flow in deformable porous media [31–33], Boutt *et al.* [34] proposed a LB discrete element method for modeling the fluid-solid mechanics in saturated deformable porous media consisting of movable rigid particles. Thereafter, Khan and Aidun [35–37] applied a parallel hybrid lattice Boltzmann–finite element method to study the deformation behavior of saturated porous media consisting of compact elastic particles or cylinders, and a link-bounce-back scheme was used to treat the fluid-solid coupling in the porous structure. These pore-scale simulation studies mainly focused on the fluid flow behaviors in deformable porous media using the LB model of momentum transfer. However, there have been few attempts to examine the mass transfer coupling adsorption and desorption processes in deformable porous media at the pore scale.

To address these issues, this work investigates the pore-scale mass transfer and desorption behaviors in deformable porous media using the LB method. Although selected LB models have been presented to study the adsorption process in nondeformable porous media [38–43], a suitable numerical scheme is still needed to describe the fluid-structure interaction at the interface between the carrier gas and the moving adsorbent particles. Different from the link-bounce-back scheme in the existing literature [35–37], an improved immersed boundary method (IBM) is introduced and combined with a three-dimensional multiple-relaxation-time (MRT)–LB model to treat the fluid-solid coupling during the desorption process. In addition, a LB model for the convection diffusion equation is applied to consider the mass transfer of adsorbate into the macropores and micropores of the porous adsorbent. This numerical model is validated using selected benchmark cases. Finally, LB simulation is performed to study the mass transfer and desorption processes in the shrinkage deformation of the porous structure caused by the movement of

rigid particles. The effects of the dynamically changing pore structure on the mass transfer and desorption efficiency are numerically illustrated in this work. This paper extends the application of the LB model for ad- and desorption processes, and offers a potential method for numerical study of the adsorption and desorption processes in deformable porous media at the pore scale.

## II. MATHEMATICAL MODELING

### A. Governing equations

Generally, a typical adsorption or desorption process contains two sections [38]. First, the fluid flow of the carrier gas and the convection diffusion of the adsorbate occur in the macropores outside of the adsorbent particles. Second, intraparticle diffusion and adsorption and desorption of the adsorbate occur in the micropores inside the adsorbent particles. In the desorption process, when the internal adsorbate molecules migrate to the external surface of the particle, the adsorbate is desorbed from the adsorbent particle and transferred into the macropores consisting of solid particles. The desorption rate at the surface is governed by adsorption kinetics theory.

In the macropores of the porous media consisting of adsorbent particles, the macroscopic governing equations for the fluid flow and mass transfer (without a source or sink term) of the adsorbate are expressed by the continuity equation, the nonsteady Navier-Stokes (NS), and the convection-diffusion equations [19], as follows:

$$\nabla \cdot \mathbf{u} = 0, \quad (1)$$

$$\frac{\partial \mathbf{u}}{\partial t} + (\mathbf{u} \cdot \nabla)(\mathbf{u}) = -\frac{1}{\rho_0} \nabla(p) + \nu \nabla^2 \mathbf{u} + \mathbf{F}, \quad (2)$$

$$\frac{\partial C_s}{\partial t} + \nabla(\mathbf{u}C_s) = D_s \nabla^2 C_s, \quad (3)$$

where  $\mathbf{u}$  and  $p$  indicate the fluid velocity and pressure, respectively;  $\rho_0$  is the fluid density;  $\nu$  is the kinetic viscosity; and  $\mathbf{F}$  is the external body force density. In Eq. (3),  $C_s$  is the concentration of the adsorbate, and  $D_s$  is the related diffusion coefficient of the adsorbate in the macropores.

In addition, the intraparticle mass transfer coupled with the adsorption and desorption behaviors are considered as intracrystalline diffusion using the homogeneous solid diffusion model (HDSM) [44]. HDSM theory assumes that the adsorbent particle with microscopic pores has a homogeneous structure. The migration of the adsorbate molecule into the adsorbent particle is achieved by “creeping” from one adsorption site to another [38]. At the mesoscale, this migration behavior in the homogeneous adsorbent particle can be described using Fick’s law, and the migration balance equation can be written as follows:

$$\frac{\partial N}{\partial t} = D_{sp} \nabla^2 N, \quad (4)$$

where  $N$  is the adsorbed phase amount per unit volume of adsorbent particle and  $D_{sp}$  is the equivalent diffusion coefficient in the adsorbent particles. The adsorption and desorption reaction at the particle surface can be described using the Langmuir adsorption kinetics model [39]. The Langmuir

adsorption kinetics approach explains adsorption by assuming the adsorption and desorption behaviors as two elementary processes. The adsorbent is considered as an ideal solid surface composed of a series of distinct sites capable of binding the adsorbate. For the adsorption process, the adsorption rate  $r_{ad}$  on the adsorbent surface is directly proportional to the adsorbate concentration over the surface  $C_{s,w}$  and the residual combined sites, where the residual combined sites can be described using the difference between the saturation adsorption amount  $N_m$  and the adsorbed phase amount at the surface  $N_w$ . As a result, the adsorption rate can be determined by Eq. (5a). The desorption rate  $r_{de}$  is directly proportional to the adsorbed phase amount at the surface, which can be described by Eq. (5b). Under the nonequilibrium state, the mass flux of adsorbate at the adsorbent surface is determined by Eq. (5c).

$$r_{ad} = k_a C_{s,w} (N_m - N_w), \tag{5a}$$

$$r_{de} = k_d N_w, \tag{5b}$$

$$D_s \frac{\partial C_{s,w}}{\partial \bar{n}} = \frac{\partial N_w}{\partial t} d\bar{n} = (r_{ad} - r_{de}) d\bar{n}, \tag{5c}$$

where  $k_a$  and  $k_d$  denote the adsorption and desorption rate constants, respectively.

**B. IBM-LB model for fluid flow**

In this work, a three-dimensional D3Q19 MRT-LB model is used to simulate the fluid flow in the macropores as described in Eqs. (1) and (2). The evolution equation can be written as [45]

$$f_i(\mathbf{x} + \mathbf{e}_i \delta t, t + \delta t) - f_i(\mathbf{x}, t) = -(\mathbf{M}^{-1} \mathbf{S} \mathbf{M})_{ij} [f_j(\mathbf{x}, t) - f_j^{eq}(\mathbf{x}, t)] + \delta t F_i \tag{6}$$

where  $f_i(\mathbf{x}, t)$  denotes the volume-averaged density distribution function at the position  $\mathbf{x}$  and the time  $t$ ,  $\delta t$  is the time step, and  $F_i$  denotes the discretized body force acting on each lattice direction which will be discussed in the following paragraphs. In addition,  $\mathbf{M}$  is an orthogonal transformation matrix of the D3Q19 scheme, and  $\mathbf{S}$  is a diagonal relaxation matrix; they are given by

$$\mathbf{M} = \begin{bmatrix} 1 & 1 & 1 & 1 & 1 & 1 & 1 & 1 & 1 & 1 & 1 & 1 & 1 & 1 & 1 & 1 & 1 & 1 \\ -30 & -11 & -11 & -11 & -11 & -11 & -11 & 8 & 8 & 8 & 8 & 8 & 8 & 8 & 8 & 8 & 8 & 8 \\ 12 & -4 & -4 & -4 & -4 & -4 & -4 & 1 & 1 & 1 & 1 & 1 & 1 & 1 & 1 & 1 & 1 & 1 \\ 0 & 1 & -1 & 0 & 0 & 0 & 0 & 1 & -1 & 1 & -1 & 1 & -1 & 1 & -1 & 0 & 0 & 0 \\ 0 & -4 & 4 & 0 & 0 & 0 & 0 & 1 & -1 & 1 & -1 & 1 & -1 & 1 & -1 & 0 & 0 & 0 \\ 0 & 0 & 0 & 1 & -1 & 0 & 0 & 1 & 1 & -1 & -1 & 0 & 0 & 0 & 0 & 1 & -1 & 1 & -1 \\ 0 & 0 & 0 & -4 & 4 & 0 & 0 & 1 & 1 & -1 & -1 & 0 & 0 & 0 & 0 & 1 & -1 & 1 & -1 \\ 0 & 0 & 0 & 0 & 0 & 1 & -1 & 0 & 0 & 0 & 0 & 1 & 1 & -1 & -1 & 1 & 1 & -1 & -1 \\ 0 & 0 & 0 & 0 & 0 & -4 & 4 & 0 & 0 & 0 & 0 & 1 & 1 & -1 & -1 & 1 & 1 & -1 & -1 \\ 0 & 2 & 2 & -1 & -1 & -1 & -1 & 1 & 1 & 1 & 1 & 1 & 1 & 1 & 1 & -2 & -2 & -2 & -2 \\ 0 & -4 & -4 & 2 & 2 & 2 & 2 & 1 & 1 & 1 & 1 & 1 & 1 & 1 & 1 & -2 & -2 & -2 & -2 \\ 0 & 0 & 0 & 1 & 1 & -1 & -1 & 1 & 1 & 1 & 1 & -1 & -1 & -1 & -1 & 0 & 0 & 0 & 0 \\ 0 & 0 & 0 & -2 & -2 & 2 & 2 & 1 & 1 & 1 & 1 & -1 & -1 & -1 & -1 & 0 & 0 & 0 & 0 \\ 0 & 0 & 0 & 0 & 0 & 0 & 0 & 1 & -1 & 1 & -1 & 0 & 0 & 0 & 0 & 0 & 0 & 0 & 0 \\ 0 & 0 & 0 & 0 & 0 & 0 & 0 & 0 & 0 & 0 & 0 & 0 & 0 & 0 & 0 & 1 & -1 & -1 & 1 \\ 0 & 0 & 0 & 0 & 0 & 0 & 0 & 0 & 0 & 0 & 0 & 1 & -1 & -1 & 1 & 0 & 0 & 0 & 0 \\ 0 & 0 & 0 & 0 & 0 & 0 & 0 & 1 & -1 & 1 & -1 & -1 & 1 & -1 & 1 & 0 & 0 & 0 & 0 \\ 0 & 0 & 0 & 0 & 0 & 0 & 0 & -1 & -1 & 1 & 1 & 0 & 0 & 0 & 0 & 1 & -1 & 1 & -1 \\ 0 & 0 & 0 & 0 & 0 & 0 & 0 & 0 & 0 & 0 & 0 & 1 & 1 & -1 & -1 & -1 & -1 & 1 & 1 \end{bmatrix}, \tag{7}$$

$$\mathbf{S} = \text{diag}(s_0, s_1, \dots, s_{18}), \tag{8}$$

$$s_0 = s_3 = s_5 = s_7 = 0, \quad s_1 = s_2 = s_{9-15} = \frac{1}{\tau}, \quad s_4 = s_6 = s_8 = s_{16-18} = 8 \frac{2\tau - 1}{8\tau - 1}, \tag{9}$$

where  $s_i (0 < s_i < 2)$  is the term of the relaxation rate, then  $\tau$  in above Eq. (9) denotes a relaxation parameter which can be used to determine the kinetic viscosity  $\nu$ :

$$\tau = \frac{\nu}{c_s^2 \delta t} + 0.5, \tag{10}$$

where  $c_s$  is the lattice sound speed. Moreover, the equilibrium distribution equation can be written as

$$f_i^{(eq)} = \omega_i \rho \left[ 1 + \frac{\mathbf{e}_i \mathbf{u}}{(c_s)^2} + \frac{(\mathbf{e}_i \mathbf{u})^2}{2(c_s)^4} - \frac{\mathbf{u} \mathbf{u}}{2(c_s)^2} \right], \quad (11)$$

where  $\omega_i$  denotes the weight coefficient of the D3Q19 model and  $\mathbf{e}_i$  denotes the discretized velocity, which are given by [46]

$$\omega_i = \begin{cases} \frac{1}{3}, & i = 0 \\ \frac{1}{18}, & 1 \leq i \leq 6 \\ \frac{1}{36}, & 7 \leq i \leq 18 \end{cases}, \quad (12)$$

$$\mathbf{e}_i = \begin{cases} (0, 0, 0) & i = 0, \\ (\pm 1, 0, 0), (0, \pm 1, 0), (0, 0, \pm 1) & 1 \leq i \leq 6, \\ (\pm 1, \pm 1, 0), (\pm 1, 0, \pm 1), (0, \pm 1, \pm 1) & 7 \leq i \leq 18, \end{cases} \quad (13)$$

The macroscopic density and viscosity of the carrier gas are given by

$$\rho = \sum_i f_i, \quad \rho \mathbf{u} = \sum_i f_i \mathbf{e}_i. \quad (14)$$

The fluid-structure interaction boundary scheme plays a key role in the accurate treatment of the moving interface between the adsorbent particle and the flow field in macropores. Fortunately, the immersed boundary method (IBM) has shown to be a powerful tool for simulating this problem [47]. In recent years, researchers have made many efforts to enhance the availability of the IBM-LB coupling scheme [48–51]. For example, Cheng *et al.* [52,53] proposed a two- (2D) and three-dimensional (3D) IBM-LB coupling method which can be applicable for flow simulation with rapid boundary motion. Then, they improved this IBM-LB scheme to overcome insufficient interpolation accuracy using an iterative force correction procedure [54]. The improvement of the IBM-LB method was demonstrated to satisfy with good accuracy at wall boundaries. As a consequence, this improved IBM-LB model is employed to implement the interaction force at the wall boundary of adsorbent particles.

In the IB scheme, the fluid flow is solved at a fixed Eulerian mesh utilizing Navier-Stokes equations as shown in Eqs. (1) and (2). Meanwhile, to describe the curvilinear boundary surrounding the surface of adsorbent particles, Lagrangian nodes  $\Gamma_b$  are set as objects immersed in the fluid. The interaction between the external body force density of fluid at Eulerian nodes and IB force density  $\mathbf{F}_{IB}$  at Lagrangian nodes is written as [55]

$$\mathbf{F}(\mathbf{x}, t) = \int_{\Gamma} \mathbf{F}_{IB}(s, t) \delta[\mathbf{x} - \mathbf{X}(s, t)] ds, \quad (15)$$

where  $\mathbf{X}$  and  $s$  denote the position and arc length of the Lagrange nodes, respectively. Moreover, the relationship between boundary velocity at Lagrangian nodes  $\mathbf{U}_{IB}$  and Eulerian velocity of fluid is expressed as

$$\mathbf{U}_{IB}(\mathbf{X}, t) = \int_{\Omega_f} \mathbf{u}(x, t) \delta[\mathbf{x} - \mathbf{X}(s, t)] d\mathbf{x}. \quad (16)$$

In the above equations, the  $\delta(r)$  is the Dirac delta function, which may be written as [53]

$$\delta(x, y, z) = \frac{1}{h^3} \phi\left(\frac{x}{h}\right) \phi\left(\frac{y}{h}\right) \phi\left(\frac{z}{h}\right), \quad (17)$$

$$\delta(r) = \begin{cases} (3 - 2|r| + \sqrt{1 + 4|r| - 4r^2})/8, & 0 \leq |r| \leq 1 \\ (5 - 2|r| + \sqrt{-7 + 12|r| - 4r^2})/8, & 1 \leq |r| \leq 2 \\ 0, & |r| \geq 2 \end{cases} \quad (18)$$

where  $h$  is the meshing space and is equal to the lattice size. Based on the discussion from previous literature [49,55],  $\Delta s$  (i.e., the arc length between two adjacent Lagrangian points) is set to be  $0.5h$  in this work. In order to introduce external force density of fluid into the LB model, the discretized body force on the right side of the LB evolution equation, Eq. (6), can be obtained using

$$F_i = \frac{1}{2} [h_i(\mathbf{x} + \mathbf{e}_i \delta t, t + \delta t) + h_i(\mathbf{x}, t)], \quad (19)$$

$$h_i = \omega_i \{A + 3\mathbf{B} \cdot [(\mathbf{e}_i - \mathbf{u}) + 3(\mathbf{e}_i \cdot \mathbf{u})\mathbf{e}_i]\}, \quad (20)$$

where  $A$  means the source term in the continuity equation and  $\mathbf{B}$  means the external forcing term in the momentum equation. Based on the above-mentioned work of Cheng *et al.* [52],  $A = 0$  and  $\mathbf{B} = \mathbf{f}$  are selected in this paper.

Furthermore, to achieve the conventional IBM-LB coupling scheme accurately, an iteration procedure is adopted to correct the external forcing term in the computational process of fluid-structure interaction [55]. In order to satisfy the nonslip boundary condition, the relationship between the desired boundary force  $\mathbf{F}_{IB}^d$  and the intermediate boundary force at the present iterative step  $\mathbf{F}_{IB}^*$  should be written as

$$\mathbf{F}_{IB}^d(\mathbf{X}, t) = \mathbf{F}_{IB}^*(\mathbf{X}, t) + 2 \frac{\mathbf{U}_{IB}^d(\mathbf{X}, t) - \mathbf{U}_{IB}^*(\mathbf{X}, t)}{\delta t}, \quad (21)$$

where  $\mathbf{U}_{IB}^d$  denotes the desired boundary velocity at the Lagrangian nodes, which is a known variable in this simulation, and  $\mathbf{U}_{IB}^*$  denotes the intermediate velocity at the present iterative step. In this iteration procedure, the intermediate boundary force at the present time step is corrected continually utilizing the intermediate boundary force and velocity at the previous time step based on Eq. (21). Then the fluid external force and fluid velocity affected by the IB boundary are recalculated by the updated intermediate boundary force, and the new intermediate velocity can be obtained from the local fluid velocity utilizing an interpolation algorithm. When the difference between the desired boundary velocity and the intermediate velocity at the present time step is less than the convergence condition or the maximum iterative number has been reached, the iteration procedure is deemed to finish. The iterative force correction method has been elaborated upon clearly in the literature [54], and the flow chart of this procedure is presented in Fig. 1.

### C. LB model for mass transfer

In this paper, a D3Q7 MRT-LB model is used to consider the mass transfer of adsorbate into the macropores and

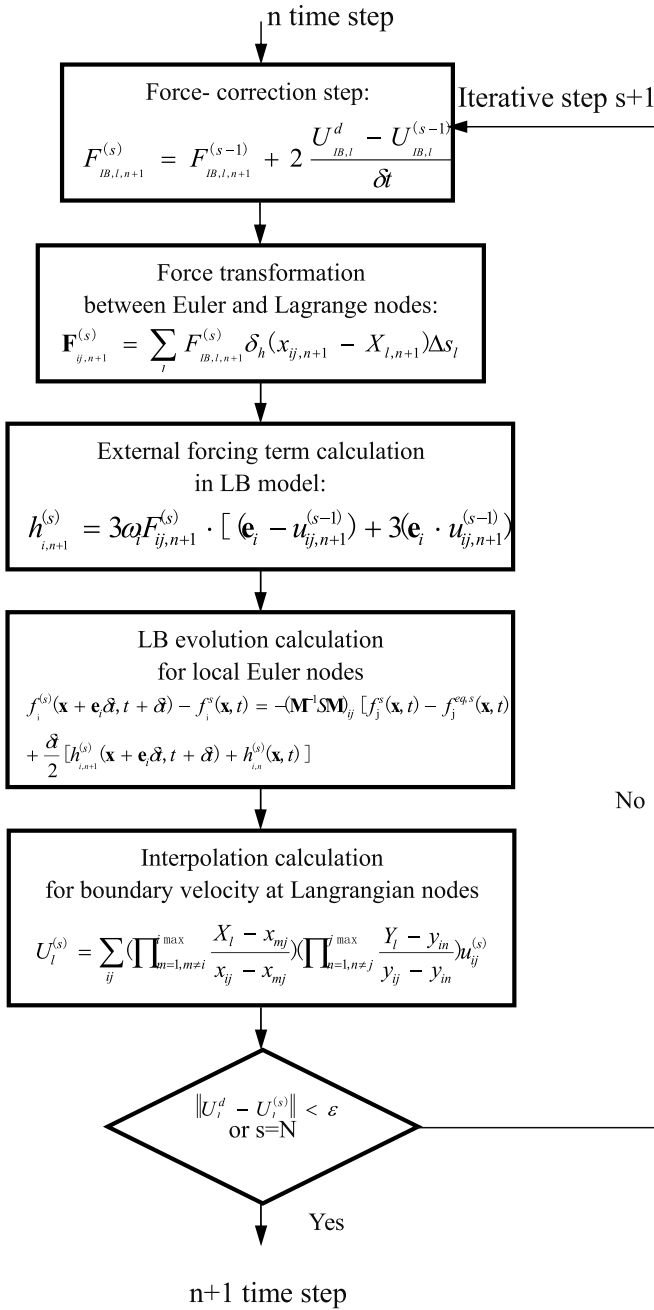


FIG. 1. Procedure of the coupled IB-LB scheme.

micropores of a porous adsorbent. The evolution equation for describing interparticle mass transport in the macropores can be written as follows [56]:

$$g_i(\mathbf{x} + \mathbf{e}_i \delta t, t + \delta t) - g_i(\mathbf{x}, t) = -(\Gamma^{-1} \Lambda \Gamma)_{ij} [g_j(\mathbf{x}, t) - g_j^{eq}(\mathbf{x}, t)], \quad (22)$$

where  $g_i(x, t)$  means the concentration distribution function of the adsorbate, and the equilibrium distribution function  $g_i^{eq}(\mathbf{x}, t)$  is given by

$$g_i^{eq}(\mathbf{x}, t) = C_s \left[ J_i + \frac{\mathbf{e}_i \cdot \mathbf{u}}{2} \right], \quad J_i = \begin{cases} J_0 & i = 0 \\ (1 - J_0)/6 & i = 1 - 6 \end{cases} \quad (23)$$

In addition,  $\Gamma$  and  $\Lambda$  in the above evolution equation are the orthogonal transformation matrix and the diagonal relaxation matrix of D3Q7 scheme, which are given by

$$\Gamma = \begin{bmatrix} 1 & 1 & 1 & 1 & 1 & 1 & 1 \\ 0 & 1 & -1 & 0 & 0 & 0 & 0 \\ 0 & 0 & 0 & 1 & -1 & 0 & 0 \\ 0 & 0 & 0 & 0 & 0 & 1 & -1 \\ 6 & -1 & -1 & -1 & -1 & -1 & -1 \\ 0 & 2 & 2 & -1 & -1 & -1 & -1 \\ 0 & 0 & 0 & 1 & 1 & -1 & -1 \end{bmatrix}, \quad (24)$$

$$\Lambda = \text{diag}(\lambda_0, \lambda_1, \dots, \lambda_6), \quad (25)$$

where  $\lambda_i$  are the relaxation rates, and  $\lambda_1 = \lambda_2 = \lambda_3 = 1/\tau_g$ . The related diffusion coefficient can be obtained using  $D_s = (1 - J_0)(\tau_g - 0.5)/3$ , and the macroscopic concentration of the adsorbate is written as follows:

$$C_s = \sum_i g_i. \quad (26)$$

Moreover, the adsorption kinetics at the surface of the particle can be considered as the Neumann boundary condition for the convection-diffusion process in macropores as shown in Eq. (5). A LB boundary scheme proposed by Zhang *et al.* [57] is employed to determine the unknown equilibrium distribution function at the wall boundary, and the distribution function entering from the outside of the surface,  $g_i^-(\mathbf{x}, t + \delta t)$ , can be given by

$$g_i^-(\mathbf{x}, t + \delta t) = -g_i^+(\mathbf{x}, t) + 2\omega_i \left( C_f + 0.5 \frac{\partial C_{s,w}}{\partial n} \delta x \bar{n} \cdot \mathbf{e}_i \right), \quad (27)$$

where  $g_i^+(\mathbf{x}, t)$  is the known distribution function entering the surface of the particle, and which is in opposite direction to the unknown distribution function  $g_i^-(\mathbf{x}, t + \delta t)$  (i.e.,  $\mathbf{e}_i = -\mathbf{e}_i$ ) [57].  $C_f$  is the concentration of adsorbate at the fluid node neighboring the surface of the particle.

On the other hand, the intraparticle mass migration can also be described as an equivalent diffusion process, and the macroscopic velocity in adsorbent particles is ignored. Hence, the above D3Q7 LB model without fluid velocity can be applied to solve the intraparticle migration balance equation as shown in Eq. (4). The transient adsorbed phase amount at the intraparticle wall boundary  $N_w$  is calculated based on the Langmuir adsorption kinetics model in Eq. (5).

#### D. Verification cases

In this section, the flow past a fixed circular cylinder at the middle of straight channel, a classic benchmark case of IBM simulation to solve fluid dynamics problems, is performed to validate the applicability of this adopted IBM-LB coupling scheme. The key dimensionless parameters used in this case are defined as follows [49]:

$$C_d = \frac{F_d}{0.5 \rho_0 U_0^2 D}, \quad C_l = \frac{F_l}{0.5 \rho_0 U_0^2 D}, \quad \text{Re} = \frac{U_0 D}{\nu}, \quad L_N = \frac{L_w}{D}, \quad (28)$$

where  $C_d$  and  $C_l$  denote the drag coefficient and the lift coefficient, respectively;  $Re$  denotes the Reynolds number as a usual dimensionless number in fluid mechanics;  $U_0$  is the fluid velocity at the inlet of the straight channel;  $D$  is the diameter of a circular cylinder;  $L_w$  is the length of the recirculation region; and  $F_d$  and  $F_l$  denote the drag force and lift force of fluid flow exerted on the fixed circular cylinder, respectively. These discretized acting forces can be derived by the following [58]:

$$F_d = - \sum_l F_{IB,x}(X_l)\Delta S_l, \quad F_l = - \sum_l F_{IB,y}(X_l)\Delta S_l. \quad (29)$$

In this simulation, the rectangular computational domain is taken as  $40D \times 20D$  for a uniform Cartesian mesh of size  $800 \times 400$ , and the circular cylinder with diameter  $D$  is located at the coordinates of  $(10D, 10D)$ , where the diameter of the circular cylinder is set as 40 lattice units. The upper

and bottom wall of the straight channel are applied as a no-slip wall boundary, the inlet fluid velocity is set to 0.1, and a free outflow boundary is applied at the outlet of this channel. These boundary schemes are implemented using the nonequilibrium extrapolation method [59]. It should be noted that the momentum transfer along the  $z$  axis in the above D3Q19 scheme is ignored to simulate this 2D benchmark case and that the numerical results are presented in the  $x$ - $y$  symmetric plane perpendicular to the  $z$  axis.

In the iteration procedure of this IBM-LB coupling scheme, the maximum number of iterations  $N$  should be appropriately selected to correct the IB force at the fluid-solid boundary. To estimate the effectiveness of this improved IB-LB scheme, the flow passing the circular cylinder is simulated using this iteration procedure with different iteration numbers  $N$  [54]. Under the computational process, the intermediate average error  $E_{ave}$  at the IB points of the cylinder wall can be defined as follows:

$$E_{ave} = \frac{\sqrt{\sum_{l=1}^{N_b} [(U_{n,x}^c - U_{n,x}^d)^2 + (U_{n,y}^c - U_{n,y}^d)^2 + (U_{n,z}^c - U_{n,z}^d)^2]}}{N_b}, \quad (30)$$

where  $U_n$  denotes the normalized velocity along orthogonal directions at the IB points,  $c$  and  $d$  denote the numerical values and the desired reference values, and  $N_b$  denotes the total number of IB points. When the Reynolds number is fixed at  $Re = 40$ , the relationship between the average error and the iteration number is plotted in Fig. 2. It can be observed that the intermediate average error decreases rapidly as a function of time and that the average error decreases with increasing iteration number. The result implies that a larger iteration number improves the accuracy of force correction at the wall boundary. At  $N = 20$ , the average error is less than  $1.0 \times 10^{-6}$ , which can be considered an acceptable error. Herein, all cases in this paper follow these selections.

It is well known that the flow regime past the fixed circular cylinder is controlled by the Reynolds number. The streamlines near the circular cylinder at different  $Re$  numbers

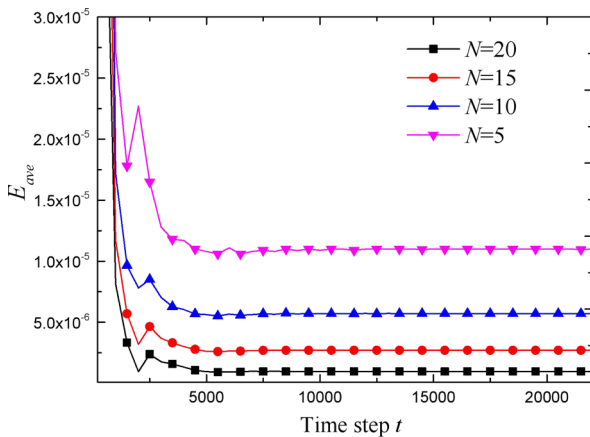


FIG. 2. Relationship between the average error and the iteration numbers.

( $Re = 20, 40, 100$ ) are shown in Fig. 3. It is found that the fluid flow remains under steady state when  $Re = 20$  and 40, and the length of the recirculation region behind the circular cylinder increases at a higher Reynolds number. However, when the Reynolds number exceeds a critical value ( $Re > 49$ ) [60], the fluid flow enters an unstable state, and the periodical von Kármán vortex is formed, as shown in Fig. 3(c). Table I compares the corresponding drag coefficient, lift coefficient, and length of the recirculation region obtained in our work with the previous literature. The results show that our results are in agreement with those previous results.

To validate the mass transfer coupling with the ad- and desorption process by taking advantage of the LB model, the mass transfer problem in a rectangular passage with an adsorption boundary at the bottom wall is simulated and compared with the analytical solution. The analogous verification case was adopted to investigate the LB model to solve the mass transfer coupling with adsorption behavior in previous studies [19,38], the schematic diagram of which is illustrated in Fig. 4(a). The side length of this rectangular passage is defined as  $L$ . The upper wall is set as a nonpermeable

TABLE I. Comparison of the results of flow around a circular cylinder.

Re	20		40		100	
	$C_d$	$L_N$	$C_d$	$L_N$	$C_d$	$C_l$
Ren <i>et al.</i> [48]	2.126	0.913	1.568	2.331	–	–
Yu <i>et al.</i> [19]	2.151	0.943	1.616	2.33	1.415	–
Tao <i>et al.</i> [49]	2.169	0.971	1.623	2.38	1.406	0.351
Linnick and Fasel [50]	2.16	0.93	1.54	2.28	1.38	0.337
Xu and Wang [51]	2.23	0.92	1.66	2.21	1.423	0.34
Present	2.172	0.933	1.556	2.203	1.451	0.342

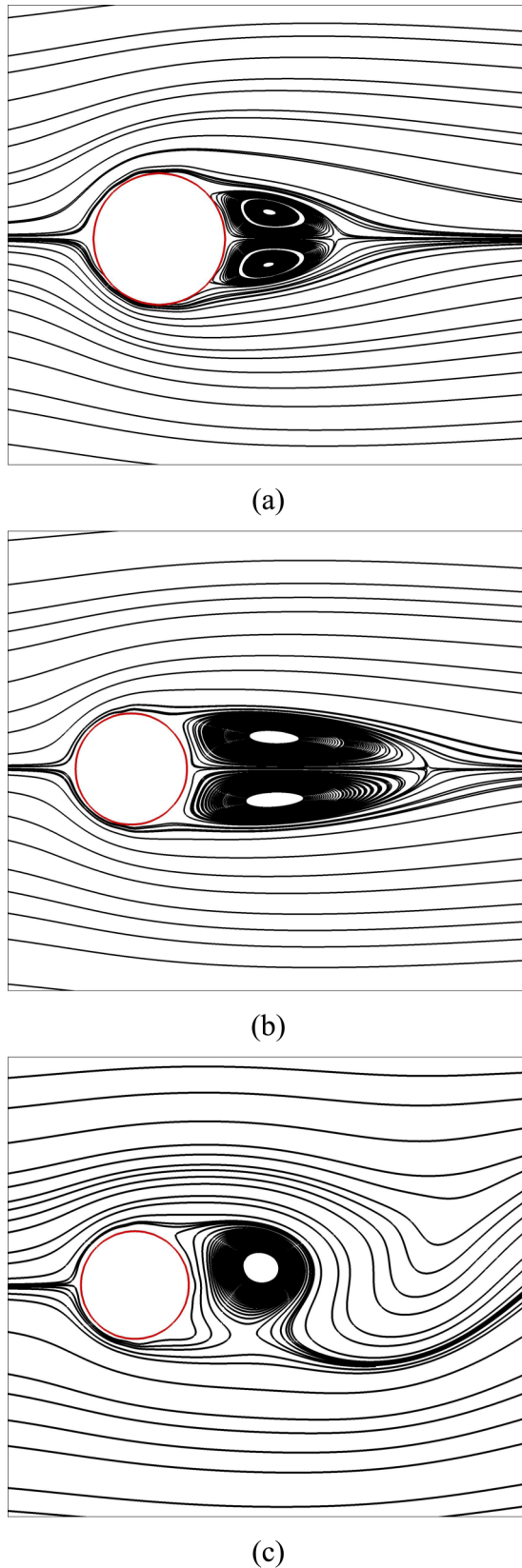
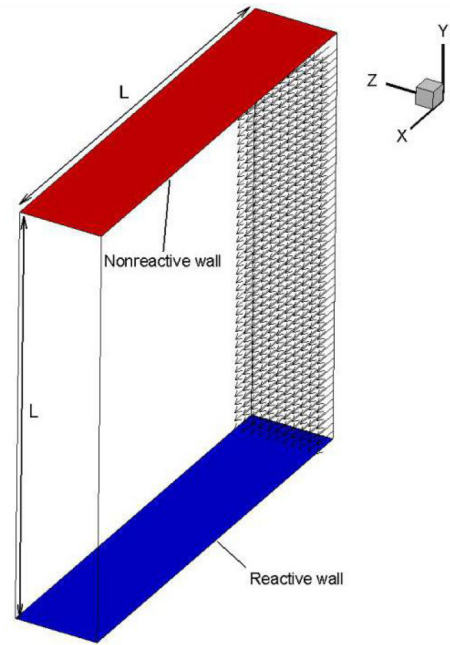
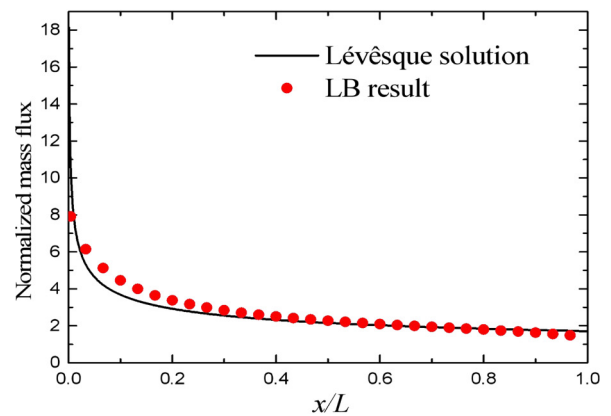


FIG. 3. The streamlines around the cylinder: (a)  $Re = 20$ ; (b)  $Re = 40$ ; (c)  $Re = 100$ .



(a)



(b)

FIG. 4. Validation case of the mass transfer problem coupled with adsorption and desorption: (a) schematic diagram of the mass transfer problem with adsorption process; (b) comparison of the LB simulation result with the Lévêsqe solution.

boundary, which means that the mass flux is zero. The bottom wall is set as the adsorption boundary, and the adsorption rate at this wall can be written as follows:

$$D_s \frac{\partial C|_{y=0}}{\partial y} = k_a C|_{y=0}, \quad (31)$$

where the adsorption rate constant  $k_a$  is imposed as 1.0 in this case and the diffusivity  $D_s$  is imposed as 0.15 in this case. Moreover, the adsorbate concentration at the inlet of the passage is imposed as  $C_0$ , and the concentration gradient is set

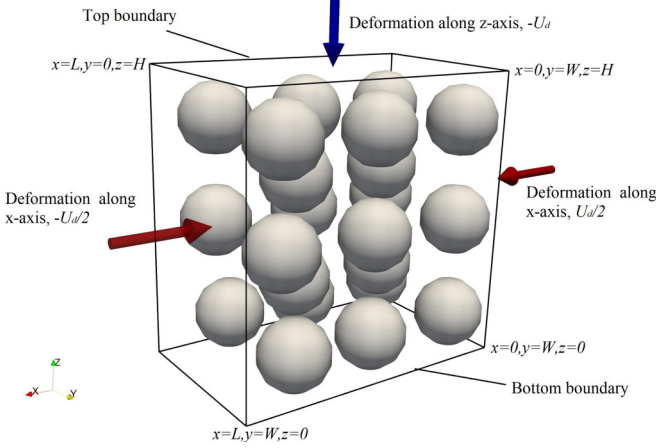


FIG. 5. Porous media structures for mass transport and desorption simulations.

as 0 at the outlet boundary using the nonequilibrium extrapolation method [59]. The flow velocity distribution along the  $y$  axis can be expressed as shown [38]:

$$u(y) = -4u_{\max}y(y - L)/L^2, \quad (32)$$

where  $u_{\max}$  denotes the maximum velocity at the axes ( $y = L/2$ ). Using LB simulation for the convection-diffusion process with  $120 \times 120 \times 30$  grids, the normalized mass flux ( $J_m$ ) at the bottom boundary along the  $x$  axis can be obtained to compare with the L ev esque solution [61], which is derived by

$$J_m = \frac{L}{C_0} \frac{\partial C}{\partial \mathbf{n}} = 0.854 \left( \frac{u_{\max} L^2}{x D_s} \right), \quad (33)$$

where the origin of  $x$  in the above equation is located at the inlet of this passage. As shown in Fig. 4(b), the normalized mass flux profile predicted by this LB model agrees with the L ev esque solution. The simulation result shows that this D3Q7 LB method can be used to model the mass transfer coupling with the ad- or desorption process.

### III. NUMERICAL DETAILS

Using the validated LB model at the pore scale, this paper investigates the mass transport and desorption processes affected by the shrinkage deformation of porous adsorbent media. As a theoretical exploration, several porous structures consisting of spherical adsorbent particles are constructed as the computational domain of this work. One of the typical porous structures is plotted as shown in Fig. 5. This porous structure consists of 22 staggered particles in a body-centered cubic arrangement, and the initial porosity is 0.77. At the initial time of this simulation (i.e., time = 0 s), the adsorbent particles have a saturation adsorption amount  $N_m$ , and the uniform initial concentration of adsorbate  $C_0$  is imposed in the macropores of the porous structure.

The deformation of the porous structure is implemented by the movement of adsorbent particles at a constant deformation speed along the  $z$  axis and the  $x$  axis. As illustrated in Fig. 5, for the porous structure deforming along the  $z$  axis, the rigid adsorbent particles at the top level move toward the bottom boundary first at the initial time of deformation, and the moving velocity is denoted as  $-U_d$ . The other particles are

TABLE II. Macroscopic boundary conditions of LB simulation.

Boundary location	Boundary conditions
$z = 0$ (Bottom boundary)	$u_{z=0} = 0, \frac{\partial P}{\partial z}  _{z=0} = 0$ $D_s \frac{\partial C}{\partial z}  _{z=0} = 0$
$z = H$ (Top boundary)	$\frac{\partial u}{\partial z}  _{z=H} = 0, p_{z=H} = P_0$ $C _{z=H} = C_0/10$
$x = 0, x = L$	$\frac{\partial u}{\partial x}  _{x=0,L} = 0$ $D_s \frac{\partial C}{\partial x}  _{x=0,L} = 0$
$y = 0, y = W$	Periodic boundary condition

driven when the upper adsorbent particles come into contact with them. On the other hand, when the porous structure deforms along the  $x$  axis, the outward adsorbent particles (i.e., the particles are close to the right and left boundaries) move toward the center of the porous structure, and the moving velocity of each particle is denoted as  $\pm U_d/2$ . It should be noted that elastic and plastic deformation are ignored for these rigid adsorbent particles and that the relative slip between the contacting particles is not considered in this work. Therefore, the contacting particles have the same speed in the shrinkage deformation process of the porous structure.

In this hypothetical porous structure, the upper wall ( $z = H$ ) is imposed as the outflow boundary of the computational domain, which means that the adsorbate desorbing from the adsorbent particles is emitted through this boundary. In this work, a sufficient mass transfer rate is assumed at the surface of the porous media. As a consequence, the adsorbate concentration of the top wall is set as the Dirichlet boundary condition ( $C_{\text{out}} = C_0/10$ , and  $C_0$  is the initial concentration). For the momentum transfer model, a constant pressure ( $P_0$ ) is imposed at this top boundary. Moreover, the bottom boundaries are imposed as nonpermeable walls of the mass transfer model and the no-slip walls for the momentum transfer simulation. The detailed macroscopic boundary conditions are presented in Table II. As mentioned above, these macroscopic boundary conditions are implemented using the nonequilibrium extrapolation method [59].

Because the lattice units of the variables are used in the LB simulation, the dimension conversion between physical units and lattice units is a necessary step for the LB model in solving an actual problem in the physical world. In this work, the realistic physical variables are taken from the literature [38,39,43], in which the adsorbate is selected as methane gas and the adsorbent particles are selected as Cu-benzene-1,3,5-tricarboxylic acid particles. Using the dimensionless transformation method, the related lattice variables in this simulation are listed in Table III, where  $\Delta N_r / \Delta x^3$  denotes the adsorbed amount per unit volume [38].

## IV. RESULTS AND DISCUSSION

### A. Desorption in nondeformable porous structure

First, based on the porous structures as shown in Fig. 5, the mass transport and desorption processes are simulated in a nondeformable porous structure (i.e.,  $U_d = 0$ ), and the transient average concentration of the adsorbate in the macropores and the average adsorption amount of particles are



TABLE III. Dimensionless lattice units and physical parameters for this simulation.

Parameter	Physical symbol	Physical value	Lattice symbol	Lattice value	Scaling relation
Grid step	$\Delta x$	$2 \times 10^{-6}$ m	$\Delta x_n$	1	$\Delta x_r = \Delta x / \Delta x_n$
Time step	$\Delta t$	$4.32 \times 10^{-8}$ s	$\Delta t_n$	1	$\Delta t_r = \Delta t / \Delta t_n$
Domain length	$L$	$2 \times 10^{-4}$ m	$L_n$	100	$L = L_n \Delta x_r$
Diameter of adsorbent particles	$D$	$4.8 \times 10^{-5}$ m	$D_n$	24	$D = D_n \Delta x_r$
Kinematic viscosity	$\nu$	$1.7 \times 10^{-5}$ m <sup>2</sup> s <sup>-1</sup>	$\nu_n$	0.1836	$\nu = \nu_n \Delta x^2 / \Delta t$
Diffusion coefficient of adsorbate	$D_s$	$4.11 \times 10^{-5}$ m <sup>2</sup> s <sup>-1</sup>	$D_{s,n}$	0.44	$D_s = D_{s,n} \Delta x^2 / \Delta t$
Equivalent diffusion coefficient in the adsorbent particles	$D_{sp}$	$1.32 \times 10^{-8}$ m <sup>2</sup> s <sup>-1</sup>	$D_{sp,n}$	$1.4 \times 10^{-4}$	$D_s = D_{sp,n} \Delta x^2 / \Delta t$
Saturation adsorption amount	$N_m$	540 mol m <sup>-3</sup>	$N_{m,n}$	1	$N_m = N_{m,n} \Delta N_r / \Delta x^3$
Initial concentration	$C_0$	0.54 mol m <sup>-3</sup>	$C_{0,n}$	0.001	$C_0 = C_{0,n} \Delta N_r / \Delta x^3$
Adsorption rate constant	$k_a$	$2.5 \times 10^3$ m <sup>3</sup> mol <sup>-1</sup> s <sup>-1</sup>	$k_{a,n}$	0.058	$k_a = k_{a,n} / (\Delta t_r \Delta N_r / \Delta x^3)$
Desorption rate constant	$k_d$	$5 \times 10^3$ s <sup>-1</sup>	$k_{d,n}$	$2.16 \times 10^{-4}$	$k_d = k_{d,n} / \Delta t_r$

reported in Fig. 6(a). As shown in this figure, the average adsorbate concentration in the porous structure increases sharply during the early stage of desorption and rapidly

reaches a peak concentration at the time of  $0.35 \times 10^{-4}$  s. The average concentration decreases as the desorption process continues, and the declining rate gradually decreases with the increase in desorption time. In contrast, the average adsorption amount decreases monotonically in the whole desorption process.

This history curve of the desorption process can be explained by the coupled mass transfer and desorption behaviors at the different time stages. At the initial time, the equilibrium adsorption concentration at the surface of the particles with the saturation adsorption amount is far greater than the initial concentration ( $C_0$ ) in the macropores. Therefore, the abundant adsorbate at the surface is quickly released into the macropores at the early stage of desorption (i.e., time less than  $0.35 \times 10^{-4}$  s). It is obvious that the desorption rate is governed by Langmuir adsorption kinetics. This desorption rate will reduce with the decreasing adsorption amount at the surface of the particles and the increasing concentration in the macropores. Because the constant concentration ( $C_{out}$ ) at the top boundary is lower than the adsorbate concentration in the macropores, the adsorbate migrates out of the porous structure under Fick's law of diffusion, and the diffusion desorption rate is determined by the effective diffusion coefficient of the adsorbate in the macropores. When the rate of adsorbate diffusing from the porous structure is greater than the desorption rate of adsorbate releasing from the particles, the concentration in the macropores decreases after the peak concentration is reached. Moreover, as the adsorption amount at the surface of the particles approaches the equilibrium state as time passes, the decreasing desorption rate decreases the adsorbate amount released into the macropores, and as a result, the adsorbate concentration declines at the later stage of desorption (i.e., time greater than  $0.35 \times 10^{-4}$  s). When the time exceeds  $0.21 \times 10^{-3}$  s, the adsorbate concentration is less than the initial concentration ( $C_0$ ), as shown in Fig. 6(a). In addition, Fig. 6(b) shows the distribution of the transient average concentration of the  $x$ - $y$  cross section along the  $z$  axis. The higher concentration gradient in the macropores is present near the top boundary, which illustrates the mass flux gradually increasing as the position of the macropores moves closer to the top boundary with a constant concentration. The three-dimensional dimensionless concentration

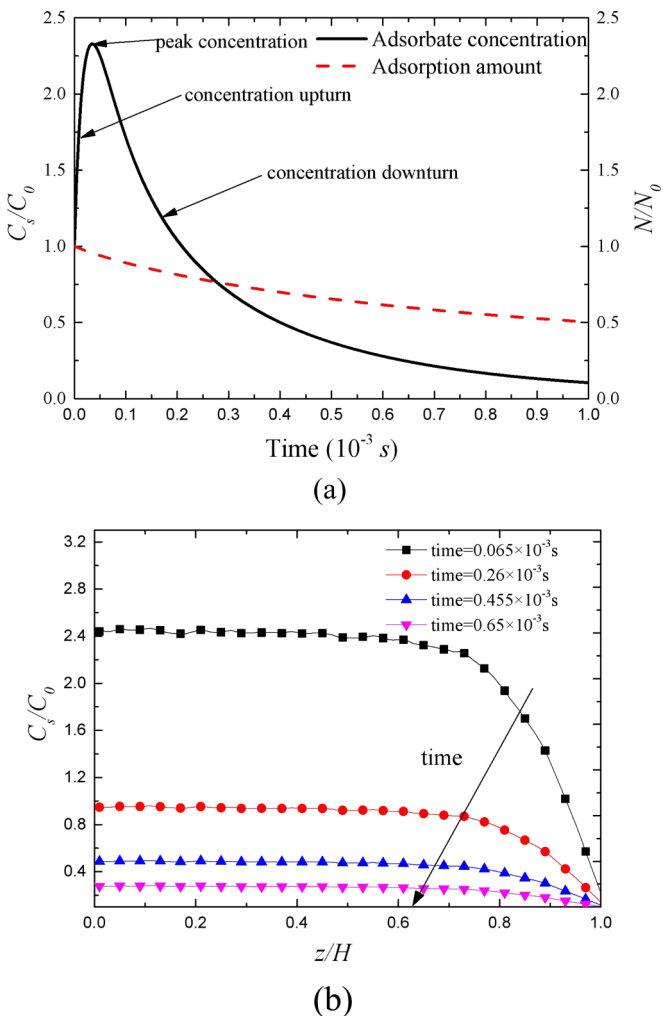


FIG. 6. The mass transport and desorption processes in nondeformable porous structure: (a) the transient average concentration of adsorbate and amount of adsorption of particles; (b) the transient average concentration distribution along the  $z$  axis.

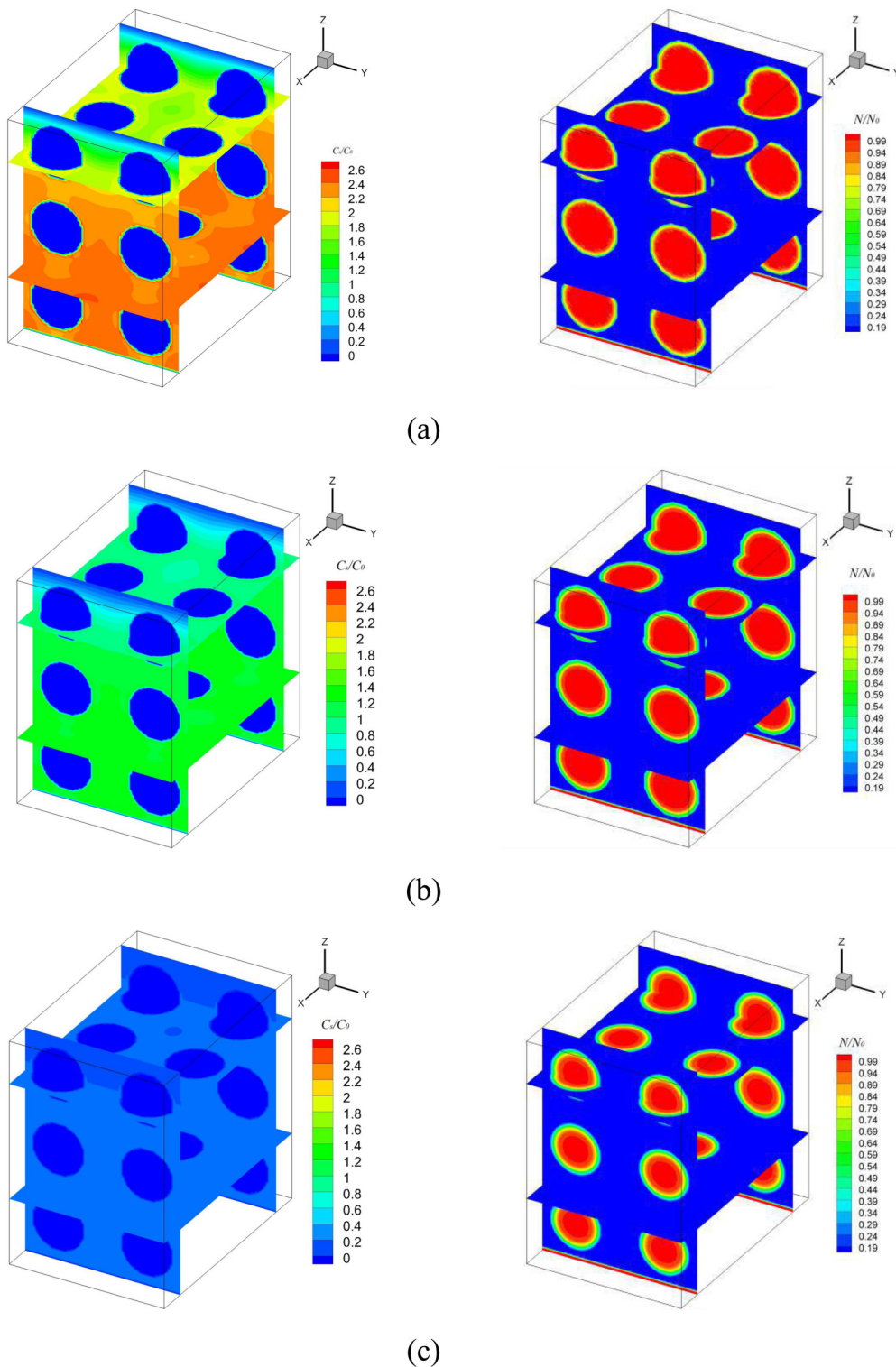


FIG. 7. The adsorbate concentration contour in macropores (left) and the adsorption amount contour inside adsorbent particles (right) in a nondeformable porous structure: (a) time =  $0.065 \times 10^{-3}$  s; (b) time =  $0.194 \times 10^{-3}$  s; (c) time =  $0.65 \times 10^{-3}$  s.

contours in the macropores are displayed in Fig. 7, showing the obvious concentration gradient profiles near the output and the decrease of concentration in the macropores with time. Moreover, Fig. 7 also shows that the adsorption gradient gradually increases along the radial direction of the adsorbent particles. These results show that the decrease-

ing adsorption amount at the surface of the particles leads to adsorbate diffusion from the center to the external surface of the particles, which is governed by the intracrystalline diffusion behavior. Due to the notably low equivalent diffusion coefficient ( $D_{sp}$ ) in the adsorbent particles compared with  $D_s$  as listed in Table III, the migration of the

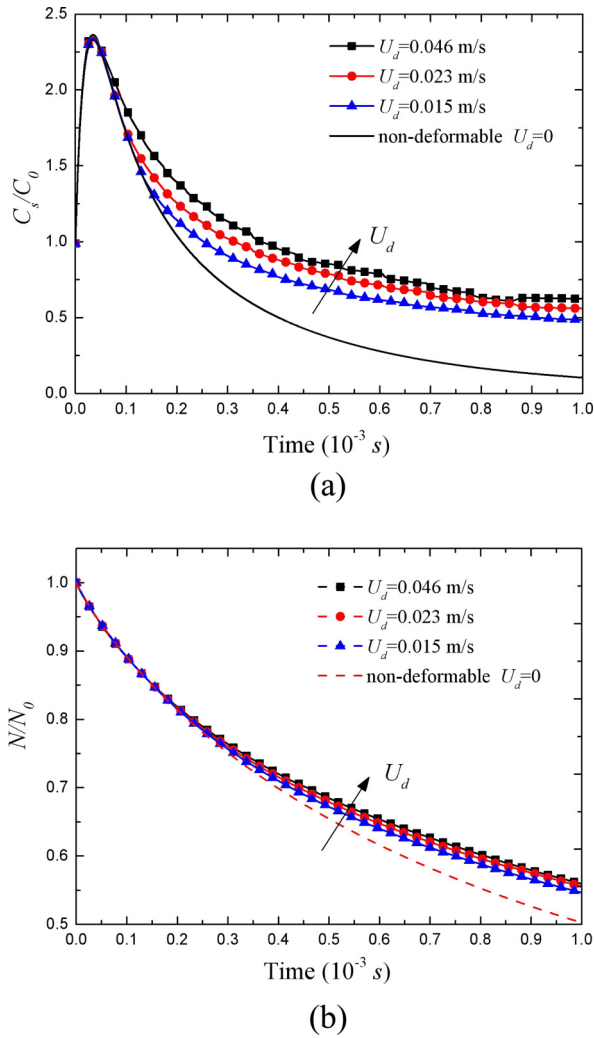


FIG. 8. The transient average concentration of adsorbate and amount of adsorption of particles in a porous structure deforming along the  $z$  axis: (a) the transient average concentration of adsorbate; (b) the transient adsorption amount of particles.

adsorbate molecules inside the particles is a notably slow process, thereby causing the concentration in the macropores and the adsorption amount inside the adsorbent particles to decline slowly at the later stage of the desorption process [39].

**B. Effects of shrinkage deformation along the  $z$  axis**

Based on the simulation results of the nondeformable porous structure, the effects of shrinkage deformation of the porous structure (as shown in Fig. 5) along the  $z$  axis (i.e., the deformation direction is opposite to the mass transport direction) on the coupled desorption processes are investigated under different velocities ( $U_d$ ). Figure 8 shows the transient average concentration of the adsorbate and amount of adsorption of particles in the porous structure deforming along the  $z$  axis. As shown in Fig. 8(a), the time history curves of the average concentration in the deformable porous structures are similar to those in the nondeformable porous structure before

the average concentration reaches the peak concentration. However, these time history curves present a significant difference in the concentration downturn period. In addition, the transient average concentration in the macropores increases with the increasing velocities of the particles. Accordingly, Fig. 8(b) reports that the decreasing rate of the average amount of adsorption of particles slows at higher particle velocities. The numerical results show that the shrinkage deformation does not have an obvious effect on the desorption process governed by the adsorption kinetics during the concentration upturn period. In the concentration downturn period, the mass transfer behavior is hindered as a result of adsorbent particles moving to the bottom boundary.

The concentration contour of the adsorbate in the macropores and the adsorption amount inside the adsorbent particles at different times are plotted in Fig. 9. The moving particles change the macroscopic pore structure and lead to the varying concentration distribution in the macropores. As the upper particles move toward the lower level, the pore sizes between them are reduced to limit the mass transfer out of the contractive pore space. As well, the isosurfaces of fluid velocity along the  $z$  axis (i.e.,  $u_z$ ) at different times are presented in the right column of Fig 9. The cyclic convection around the moving adsorbent particles is obvious. Furthermore, the intensity of this convection can be described quantitatively using the local Péclet number (i.e.,  $Pe_L$ ) as follows:

$$Pe_L = \frac{L|U_f|}{D}, \tag{34}$$

where  $U_f$  denotes the fluid velocity. Figure 10 plots the local Péclet number along the  $z$  axis at different times. It can be observed that the moving particles cause a higher convection zone during the shrinkage deformation process. With the downward movement of the adsorbent particles, the peak Péclet number also shifts toward the bottom boundary. Moreover, Figs. 10(a)–10(c) imply that the role of convection is distinctly enhanced with an increase in the moving velocity of the particles. As shown in Fig. 9, due to the downward movement of the adsorbent particles, the fluid surrounding these moving particles forms convection toward the bottom boundary under the role of solid-fluid coupling. On the other hand, under the role of cyclic convection, there are small regions away from moving particles in which the fluid flows in the positive  $z$  direction. It should be mentioned that the regions near the moving particles have the higher adsorbate concentration and the larger flow velocity of carrier gas in the opposite direction to the top boundary. As a result, this convection surrounding these moving particles improves the mass transport resistance in the desorption process, and thus the higher concentration zone can be observed below the moving particle level. The effect of the deformation of the pore structure on the detailed transient concentration distributions in the macropores along the  $z$  axis are illustrated in Fig. 11. The transient concentrations along the  $z$  axis present a higher concentration zone caused by the deformation of the pore structure, and the peak concentration of this higher concentration zone slips toward the bottom boundary ( $z = 0$ ) with the downward movement of the adsorbent particles. Moreover, the higher concentration in the macropores gives rise to a higher equilibrium concentration at the surface of

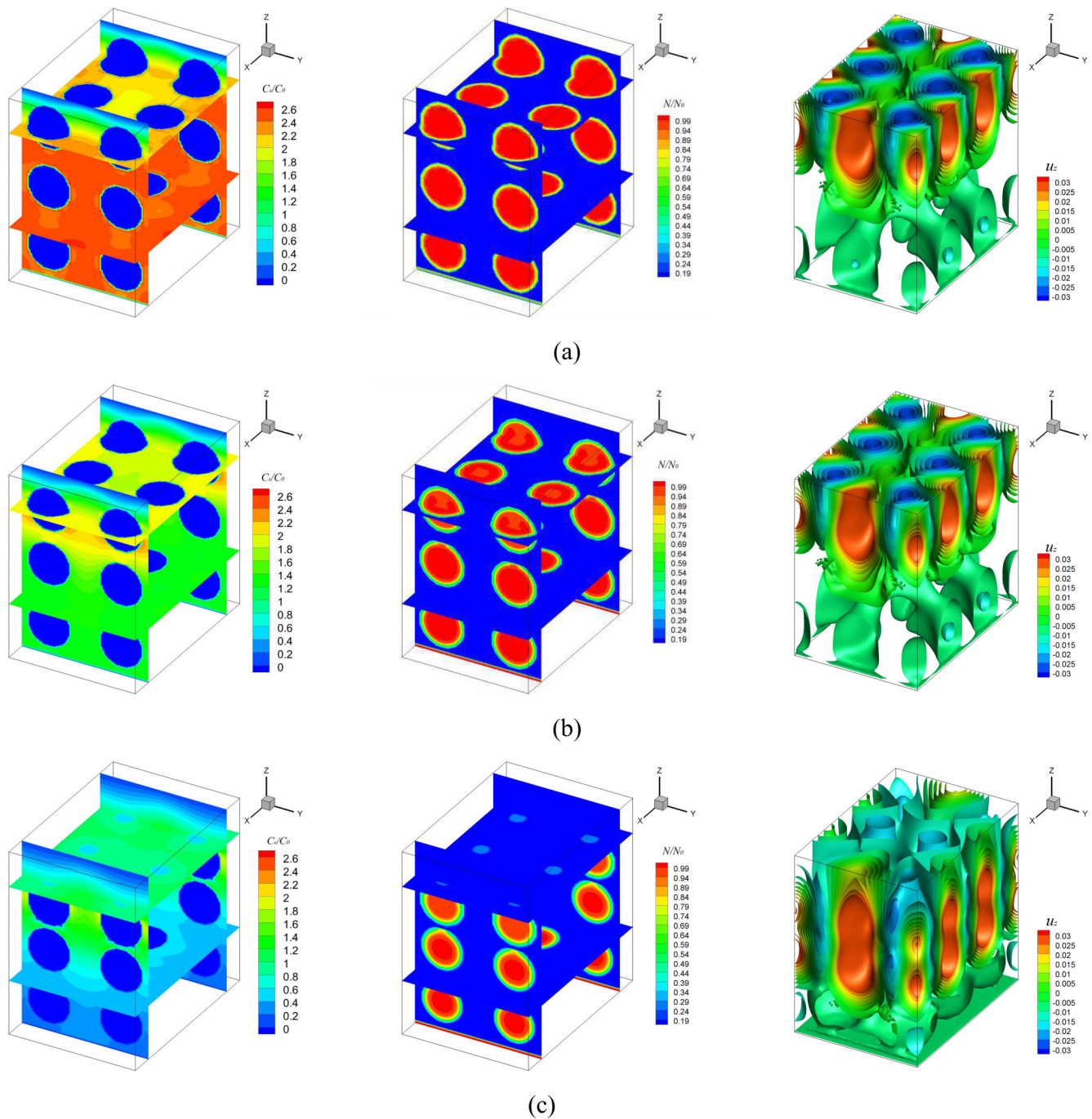


FIG. 9. The adsorbate concentration contour in macropores (left), the adsorption distribution inside adsorbent particles (middle), and the isosurfaces of fluid velocity  $u_z$  (right) in porous structure deforming along the  $z$  axis ( $U_d = 0.046$  m/s): (a) time =  $0.065 \times 10^{-3}$  s; (b) time =  $0.194 \times 10^{-3}$  s; (c) time =  $0.65 \times 10^{-3}$  s.

the adsorbent particles. Therefore, the desorption process and mass migration inside the particles are slowed by the shrinkage deformation of the pore structure during the concentration downturn period.

### C. Effects of shrinkage deformation along the $x$ axis

Furthermore, this numerical model is used to study the mass transport and desorption processes in the porous

structure deforming along the  $x$  axis (i.e., the deformation direction is perpendicular to the mass transport direction) under the same operation condition. Figure 12 presents the effect of deformable velocity on the transient average concentration of the adsorbate and the amount of adsorption of particles in the porous structure. At the early stage of desorption, the transient average concentrations in the deformable porous structure match those in the nondeformable porous structure. Although the dynamic deformation of the adsorbent particles leads to

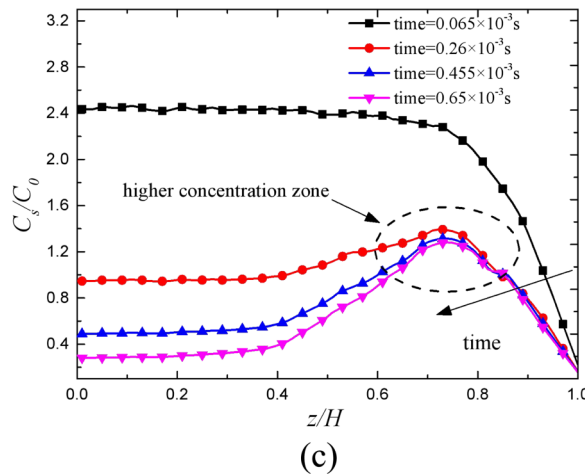
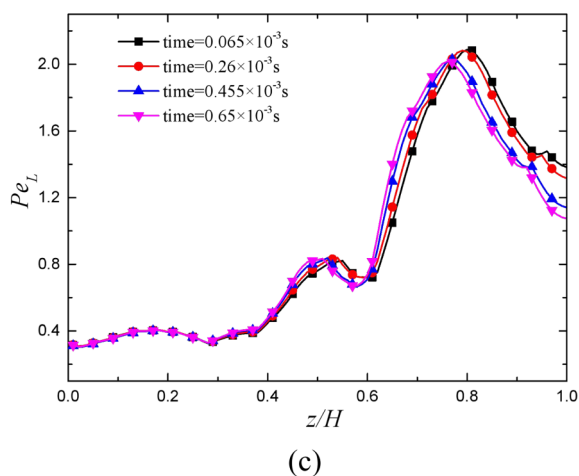
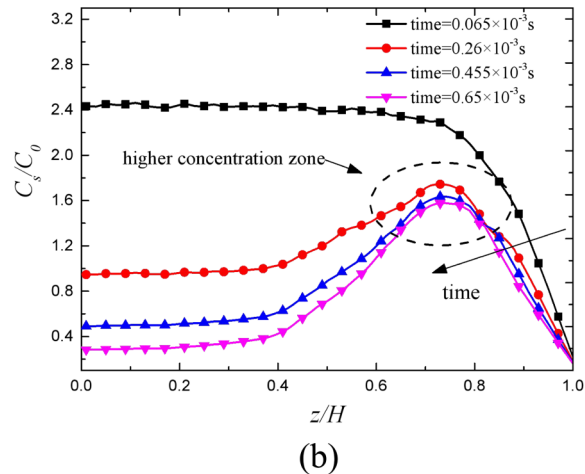
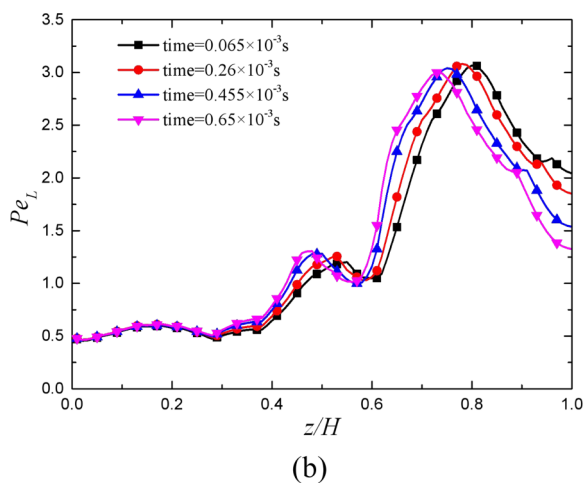
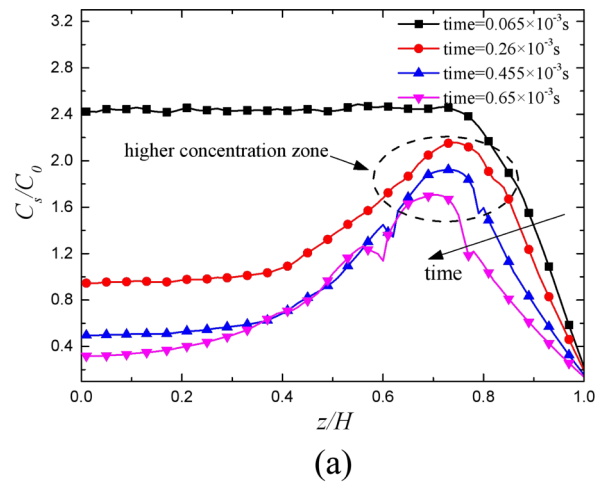
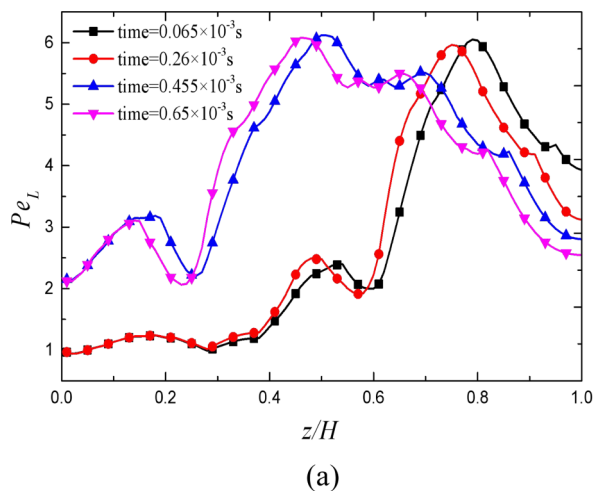


FIG. 10. The local Péclet number along the  $z$  axis when the porous structure deforms along the  $z$  axis: (a)  $U_d = 0.046$  m/s; (b)  $U_d = 0.023$  m/s; (c)  $U_d = 0.015$  m/s.

FIG. 11. The transient average concentration distribution along the  $z$  axis when the porous structure deforms along the  $z$  axis: (a)  $U_d = 0.046$  m/s; (b)  $U_d = 0.023$  m/s; (c)  $U_d = 0.015$  m/s.

fluid flow (as shown in the isosurface profiles in the right column of Fig. 13), the effect of this convection on the mass transport and desorption behaviors is inconspicuous during the concentration upturn period. However, the decreasing rate of concentration shows a significant difference in porous

structures with varying moving velocity of particles at the later stage of desorption, owing to the shrinkage deformation along the  $x$  axis changing the structure of the macropores and observably reducing the effective diffusion coefficient of the adsorbate in the macropores. As shown in Fig. 13, the distance along the  $x$  axis between two particles is shortened

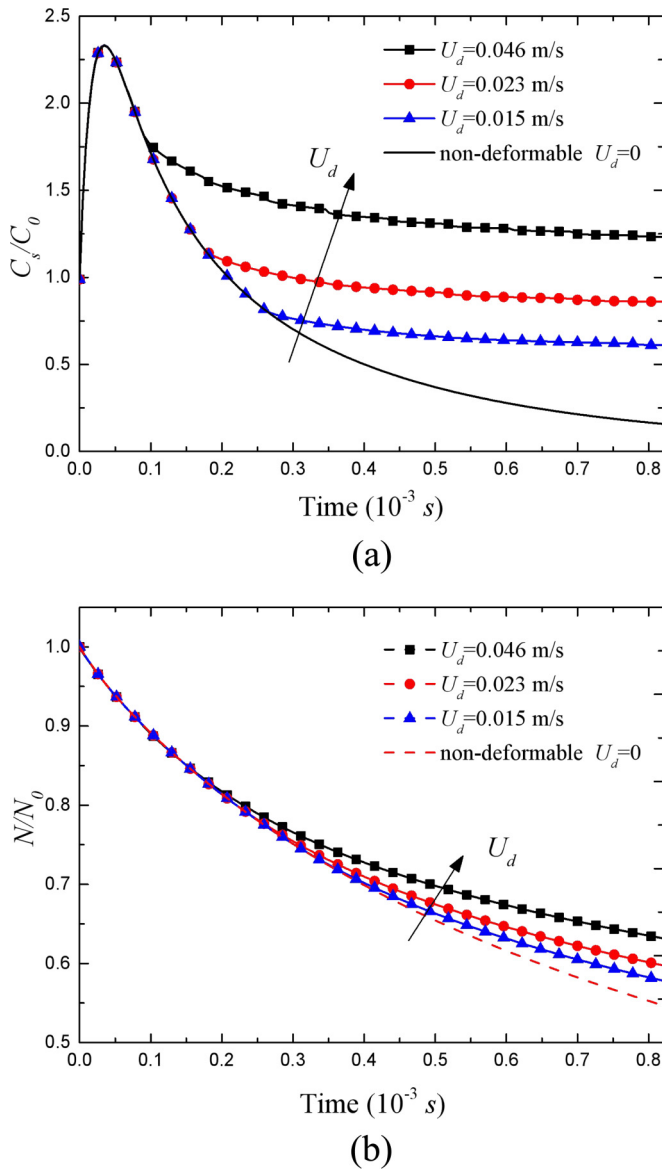


FIG. 12. The transient average concentration of adsorbate and amount of adsorption of particles in a porous structure deforming along the  $x$  axis: (a) the transient average concentration of adsorbate; (b) the transient adsorption amount of particles.

during the deformation process. Because the adsorbate migrates along the  $z$  axis, the pores in the  $x$ - $y$  cross section are the primary mass transfer channels. When the direction of the shrinkage deformation is perpendicular to the mass transport direction, these primary mass transfer channels are blocked. Consequently, the mass transfer resistance is greatly improved and hinders the diffusion of the adsorbate in the macropores. Figure 14 plots the detailed transient concentration distributions in the macropores as the porous structure deforms along the  $x$  axis. The results show that this concentration distribution is different from that shown in Fig. 11. The concentration of the adsorbate decreases as the position of the macropores is located closer to the top boundary, and the higher concentration zone is not evident in the macropores. The decreasing rate of the overall concentration distribution declines as the size of

the pore channels is decreased during shrinkage deformation, thereby leading to retardation of the desorption process. As a consequence, the transient adsorption amount of adsorbent particles is improved at a higher particle moving velocity at the later stage of desorption, as shown in Fig. 12(b).

In addition, the numerical results show that the declining rate of the adsorbate concentration in porous media deforming along the  $x$  axis is lower than that along the  $z$  axis at the later stage of desorption under the same operation condition. To illustrate the role of the deformation direction in the dynamic desorption process, the transient residual adsorption amounts inside the adsorbent particles are compared under different deformation directions and particle moving velocities. Figure 15 shows that the residual adsorption amount in the porous structure deforming along the  $x$  axis is less than that along the  $z$  axis at the lower particle moving velocity ( $U_d = 0.015$  m/s), and the gap between them decreases as time passes. In contrast, an inverse trend is presented at the higher particle moving velocity ( $U_d = 0.046$  m/s). The higher residual adsorption amount inside the adsorbent particles is due to the decreasing mass transfer rate in the macropores subdued by the shrinkage deformation of the porous media. As a result, compared with the deformation along the  $z$  axis, the adverse effect of the particle velocity on the efficiency of the desorption process becomes more apparent when the porous structure deforms along the  $x$  axis.

#### D. Effects of morphology of porous structures

The above simulations are performed using a fixed initial porous structure. In this section, the mass transfer and desorption behaviors are compared in porous media with different initial morphologies. The porous structure plotted in Fig. 5 is denoted as case 1 in this section. As explained above, case 1 consists of adsorbent particles in a body-centered cubic arrangement, the initial porosity of which is approximately equal to 0.77, as shown in Fig. 16(a). In addition, two other porous structures are constructed and denoted as case 2 and case 3. Case 2 consists of granular adsorbent particles in a simple cubic arrangement, and the initial porosity is equal to 0.81, as shown in Fig. 16(b). Case 3 consists of adsorbent particles in a staggered arrangement, and the initial porosity is also equal to 0.81, as shown in Fig. 16(c).

Under the fixed moving velocity of the adsorbent particles ( $U_d = 0.023$  m/s) along the  $z$  axis, the mass transfer and desorption processes are simulated in the different initial porous structures. Figure 17(a) shows the time history curves of the average adsorbate concentration in the porous structures of cases 1–3. The result presents a significant difference in peak concentration affected by the morphology of the porous structure. Due to the lower porosity and larger total adsorption capacity, the porous structure of case 1 has a higher desorption rate and lower effective diffusivity, thus resulting in a higher transient adsorbate concentration. However, although it has the same porosity and total adsorption capacity as the porous structures of cases 2 and 3, case 3 presents a lower peak concentration at the early stage of desorption. The reason for this observation might be attributed to the difference in local porosity between case 2 and case 3. At the early stage of desorption, the concentration gradient appears mainly in

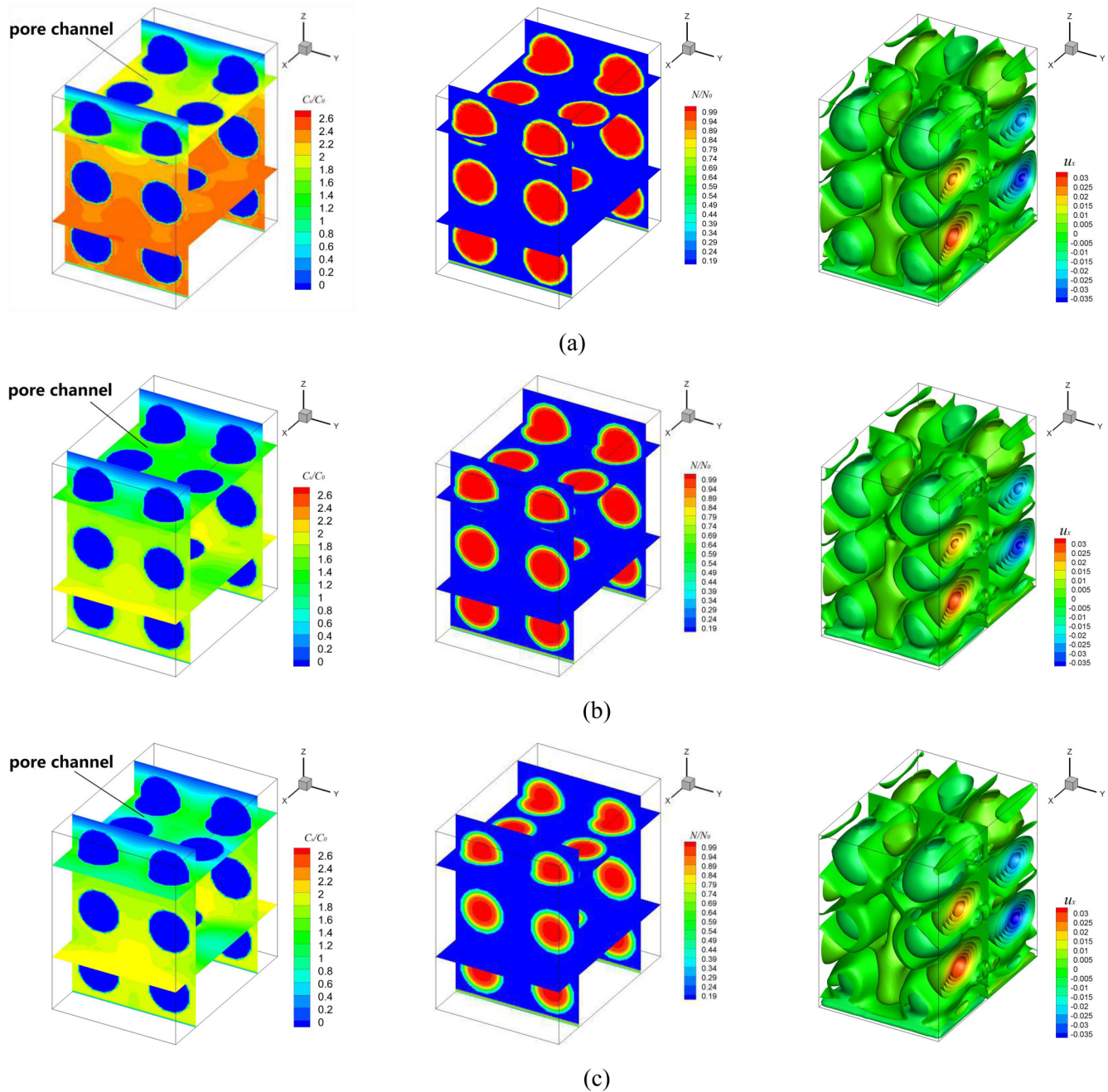


FIG. 13. The adsorbate concentration contour in macropores (left), the adsorption distribution inside adsorbent particles (middle), and the isosurfaces of fluid velocity  $u_x$  (right) in porous structure deforming along the  $x$  axis ( $U_d = 0.046$  m/s): (a) time =  $0.065 \times 10^{-3}$  s; (b) time =  $0.194 \times 10^{-3}$  s; (c) time =  $0.65 \times 10^{-3}$  s.

the top of the porous structure. Due to the least number of adsorbent particles at the top level of case 3, the larger local porosity in the top of the porous structure leads to a higher mass transfer rate and a lower peak concentration during the concentration upturn period.

In contrast, the transient adsorbate concentration in the porous structure of case 3 is higher than that of case 2 during the concentration downturn period. In other words, the mass transfer rate in case 3 is less than that in case 2 as the porous structure deforms along the  $z$  axis. This result might be attributed to the different morphologies of the porous

structures. In general, the staggered arrangement of adsorbent particles could lead to a higher tortuosity of the porous structure, thereby improving the mass transfer resistance in the porous media. Moreover, during the shrinkage deformation process, compared with the porous structure with a simple cubic arrangement (i.e., case 2), the shrinkage of the nonuniform and curving pore channels in cases 1 and 3 is likely to cause blocking of the macropores and further hinder the mass transfer of adsorbate out of the porous media. On the other hand, case 2 presents a lower transient concentration in the macropores at the later stage of the desorption process due to

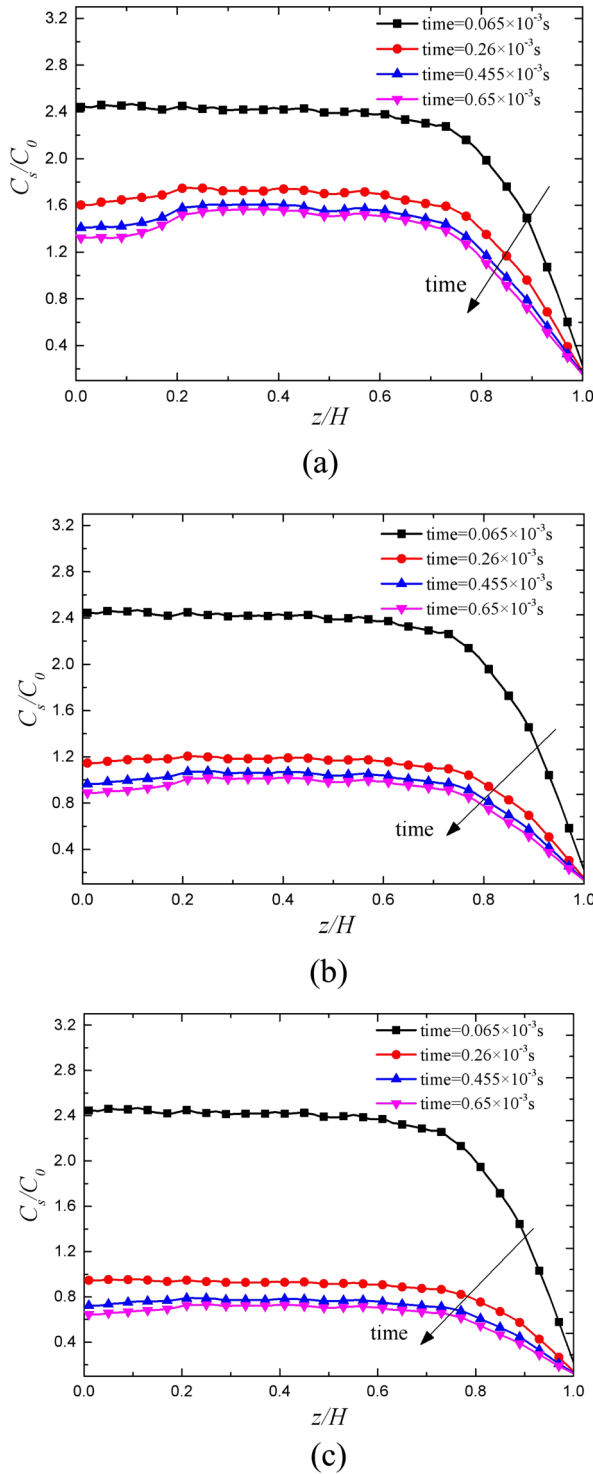


FIG. 14. The transient average concentration distribution when the porous structure deforms along the  $x$  axis: (a)  $U_d = 0.046$  m/s; (b)  $U_d = 0.023$  m/s; (c)  $U_d = 0.015$  m/s.

the lower mass transfer resistance in the porous structure with a simple cubic arrangement. As a result, the lower adsorbate concentration in the macropores contributes to improving the desorption rate of the adsorbent particles, thus reducing the amount of transient adsorption of particles for case 2 at the later stage of desorption, as shown in Fig. 17(b).

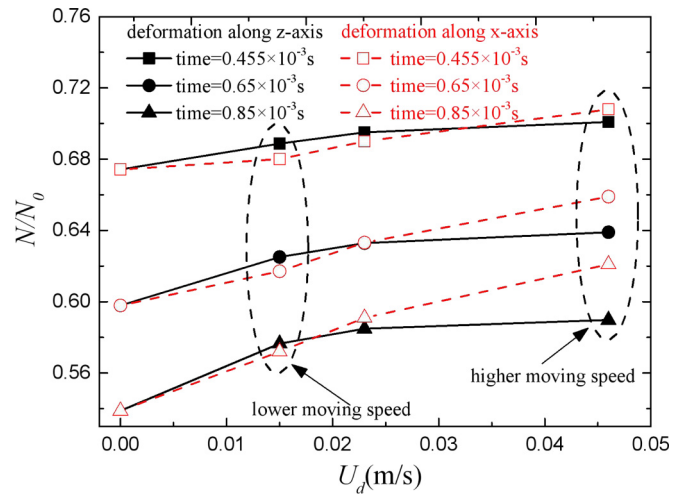


FIG. 15. The role of deformation direction on desorption process.

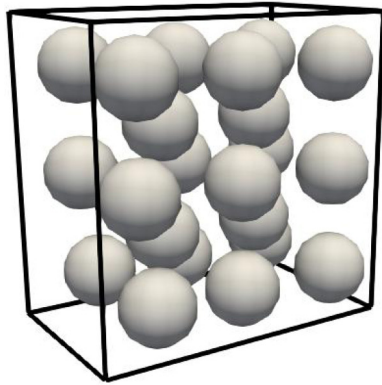
V. CONCLUSION

A coupling IBM-LB model is proposed to investigate the mass transfer and desorption behaviors in deformable porous media. The applicability of this MRT-LB model is validated using selected classic benchmark cases and comparison with the results from the literature. Based on the validated IBM-LB model, numerical simulations are performed to study the mass transfer and desorption processes in shrinkage deformation of a porous structure caused by the movement of rigid adsorbent particles along different directions. The results show that the time history curve of the adsorbate concentration in the macropores can be divided into the upturn period and the downturn period during the dynamic desorption process. During the concentration upturn period governed by Langmuir adsorption kinetics, the effects of the shrinkage deformation of the porous structure along different directions on the desorption behavior are not distinct. However, during the concentration downturn period governed by the mass transfer rate of the adsorbate, the shrinkage deformation of the porous structure obviously decreases the rate of the desorption process.

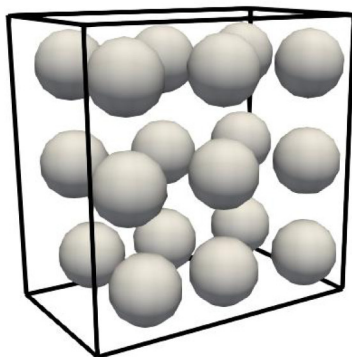
When the deformation direction is opposite to the direction of mass transport (i.e., along the  $z$  axis), the contractive pore space limits the mass transfer rate of the adsorbate in the macropores. At the same time, due to the downward movement of the adsorbent particles, the convection around the particles flowing in the direction opposite to the outlet of the porous structure results in increasing mass transport resistance in the desorption process. As a result, a higher concentration zone can be observed below the moving particle level, leading to the decreased desorption rate during the concentration downturn period.

As the deformation direction is perpendicular to the mass transport direction (i.e., along the  $x$  axis), the size of the primary pore channels of mass transfer in the  $x$ - $y$  cross section is obviously reduced. Consequently, the mass transfer resistance is greatly improved, thus hindering the diffusion of adsorbate in macropores and distinctly causing retardation of the desorption process during the concentration downturn period. Compared with the deformation along the  $z$  axis, the

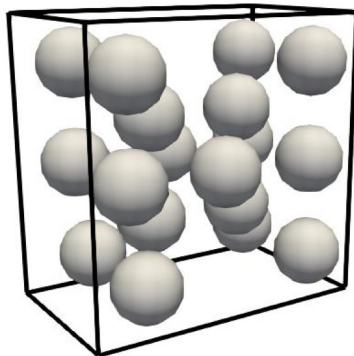




(a)



(b)

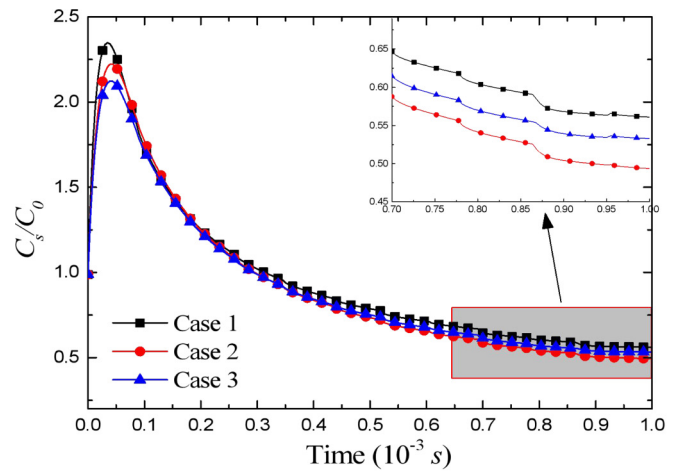


(c)

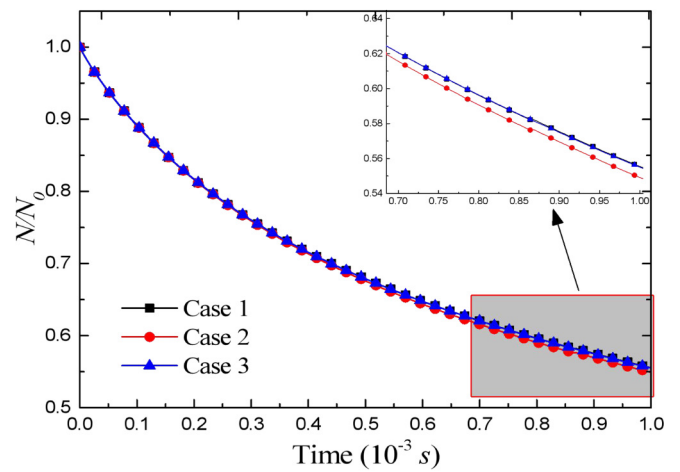
FIG. 16. The porous structures with different initial morphology: (a) case 1 (porosity of 0.77, body-centered cubic arrangement); (b) case 2 (porosity of 0.81, simple cubic arrangement); (c) case 3 (porosity of 0.81, staggered arrangement).

adverse effect of shrinkage deformation on the efficiency of the desorption process is more significant than in the porous structure deforming along the  $x$  axis.

In addition, a comparative simulation is performed to investigate the mass transfer and desorption behaviors in porous media with different morphologies. Under the same porosity



(a)



(b)

FIG. 17. The transient average concentration of adsorbate and adsorption amount of particles in porous structures with different morphology deforming along the  $z$  axis: (a) the transient average concentration of adsorbate; (b) the transient adsorption amount of particles.

and moving velocity of the absorbent particles, the porous structure with a staggered arrangement of absorbent particles presents a higher mass transfer resistance, thus decreasing the desorption rate during the shrinkage deformation process.

### ACKNOWLEDGMENTS

This work is fully supported by National Natural Science Foundation of China (Grants No. 51806083 and No. 51676037), China Postdoctoral Science Foundation (Grant No. 2018M632242), Natural Science Foundation of Jiangxi Province (Grant No. 20192BAB216027), and High-Tech Research Key Laboratory of Zhenjiang City (Grant No. SS2018002). We would also like to thank Dr. Prabhu Raj Balakrishnan for helpful discussions.

- [1] I. Vlahinić, H. M. Jennings, and J. J. Thomas, A constitutive model for drying of a partially saturated porous material, *Mech. Mater.* **41**, 319 (2009).
- [2] F. Putz, A. Waag, C. Balzer, S. Braxmeier, M. S. Elsaesser, L. Ludescher, P. Oskar, G. R. M. J. Wim, and H. Nicola, The influence of drying and calcination on surface chemistry, pore structure and mechanical properties of hierarchically organized porous silica monoliths, *Microporous Mesoporous Mater.* **288**, 109578 (2019).
- [3] Z. Zhang, Y. Fang, and X. Du, 3D transport of solute in deformable soils with different adsorption modes, *Soil Mech. Found. Eng.* **54**, 128 (2017).
- [4] Z. Pan and L. D. Connell, A theoretical model for gas adsorption-induced coal swelling, *Int. J. Coal Geol.* **69**, 243 (2007).
- [5] D. N. Espinoza, M. Vandamme, J.-M. Pereira, P. Dangla, and S. Vidal-Gilbert, Measurement and modeling of adsorptive-poromechanical properties of bituminous coal cores exposed to CO<sub>2</sub>: Adsorption, swelling strains, swelling stresses and impact on fracture permeability, *Int. J. Coal Geol.* **134–135**, 80 (2014).
- [6] O. L. Manzoli, P. R. Cleto, M. Sánchez, L. J. N. Guimarães, and M. A. Maedo, On the use of high aspect ratio finite elements to model hydraulic fracturing in deformable porous media, *Comput. Methods Appl. Mech. Eng.* **350**, 57 (2019).
- [7] A. Grosman and C. Ortega, Influence of elastic deformation of porous materials in adsorption-desorption process: A thermodynamic approach, *Phys. Rev. B* **78**, 085433 (2008).
- [8] D. Mihoubi and A. Bellagi, Modeling of heat and moisture transfers with stress-strain formation during convective air drying of deformable media, *Heat Mass Transfer* **48**, 1697 (2012).
- [9] L. Bennamoun, L. Fraikin, and A. Léonard, Modeling and simulation of heat and mass transfer during convective drying of wastewater sludge with introduction of shrinkage phenomena, *Drying Technol.* **32**, 13 (2013).
- [10] V. Nicolas, P. Salagnac, P. Glouannec, J. P. Ploteau, V. Jury, and L. Boillereaux, Modelling heat and mass transfer in deformable porous media: Application to bread baking, *J. Food Eng.* **130**, 23 (2014).
- [11] T. Lu, H. L. Wang, and P. X. Jiang, A thermo-hydro-mechanics bidirectional coupling mathematical model for drying of biological porous medium, *Drying Technol.* **33**, 420 (2015).
- [12] J. Siddique, A. Ahmed, A. Aziz, and C. Khalique, A review of mixture theory for deformable porous media and applications, *Appl. Sci.* **7**, 917 (2017).
- [13] A. Gajo, F. Cecinato, and B. Loret, A computational framework for immiscible three-phase flow in deformable porous media, *J. Pet. Sci. Eng.* **165**, 516 (2018).
- [14] B. Detmann and P. Krejčí, A multicomponent flow model in deformable porous media, *Math Methods Appl. Sci.* **42**, 1894 (2019).
- [15] M. B. Albro, R. Li, R. E. Banerjee, C. T. Hung, and G. A. Ateshian, Validation of theoretical framework explaining active solute uptake in dynamically loaded porous media, *J. Biomech.* **43**, 2267 (2010).
- [16] L. Yang, A mixed element method for the desorption-diffusion-seepage model of gas flow in deformable coalbed methane reservoirs, *Math. Probl. Eng.* **2014**, 735931 (2014).
- [17] Y. Zhang, Mechanics of adsorption-deformation coupling in porous media, *J. Mech. Phys. Solids* **114**, 31 (2018).
- [18] M. R. Hajiabadi and A. R. Khoei, A bridge between dual porosity and multiscale models of heterogeneous deformable porous media, *Int. J. Numer. Anal. Methods Geomech.* **43**, 212 (2018).
- [19] X. Yu, K. Regenauer-Lieb, and F.-B. Tian, A hybrid immersed boundary-lattice Boltzmann/finite difference method for coupled dynamics of fluid flow, advection, diffusion and adsorption in fractured and porous media, *Comput. Geosci.* **128**, 70 (2019).
- [20] C. Balzer, T. Wildhage, S. Braxmeier, G. Reichenauer, and J. P. Olivier, Deformation of porous carbons upon adsorption, *Langmuir* **27**, 2553 (2011).
- [21] R. Diao, C. Fan, D. D. Do, and D. Nicholson, Adsorption induced deformation in graphitic slit mesopores: A Monte Carlo simulation study, *Chem. Eng. J.* **328**, 280 (2017).
- [22] V. K. Shen, D. W. Siderius, and N. A. Mahynski, Molecular simulation of capillary phase transitions in flexible porous materials, *J. Chem. Phys.* **148**, 124115 (2018).
- [23] Z. Chai, X. Guo, L. Wang, and B. Shi, Maxwell-Stefan-theory-based lattice Boltzmann model for diffusion in multicomponent mixtures, *Phys. Rev. E* **99**, 023312 (2019).
- [24] Q. Liu, X.-B. Feng, X.-T. Xu, and Y.-L. He, Multiple-relaxation-time lattice Boltzmann model for double-diffusive convection with Dufour and Soret effects, *Int. J. Heat Mass Transfer* **139**, 713 (2019).
- [25] B. Chen, L. Song, K. Gao, and F. Liu, Two zone model for mushy region of solid-liquid phase change based on lattice Boltzmann method, *Int. Commun. Heat Mass Transfer* **98**, 1 (2018).
- [26] L. Wang, W. Zhao, and X.-D. Wang, Lattice kinetic scheme for the Navier-Stokes equations coupled with convection-diffusion equations, *Phys. Rev. E* **98**, 033308 (2018).
- [27] W. Zhou, Y. Yan, X. Liu, H. Chen, and B. Liu, Lattice Boltzmann simulation of mixed convection of nanofluid with different heat sources in a double lid-driven cavity, *Int. Commun. Heat Mass Transfer* **97**, 39 (2018).
- [28] H. Xu and Z. Xing, The lattice Boltzmann modeling on the nanofluid natural convective transport in a cavity filled with a porous foam, *Int. Commun. Heat Mass Transfer* **89**, 73 (2017).
- [29] L. Chen, Q. Kang, Q. Tang, B. A. Robinson, Y.-L. He, and W.-Q. Tao, Pore-scale simulation of multicomponent multiphase reactive transport with dissolution and precipitation, *Int. J. Heat Mass Transfer* **85**, 935 (2015).
- [30] J. Li, F. Hong, R. Xie, and P. Cheng, Pore scale simulation of evaporation in a porous wick of a loop heat pipe flat evaporator using lattice Boltzmann method, *Int. Commun. Heat Mass Transfer* **102**, 22 (2019).
- [31] H. El Abrach, H. Dhahri, and A. Mhimid, Numerical simulation of drying of a deformable anisotropic porous medium using the lattice Boltzmann method, *Drying Technol.* **31**, 1400 (2013).
- [32] H. El Abrach, H. Dhahri, and A. Mhimid, Lattice Boltzmann method for modelling heat and mass transfers during drying of deformable porous medium, *J. Porous Media* **16**, 837 (2013).
- [33] H. El Abrach, H. Dhahri, and A. Mhimid, Numerical simulation of drying of a saturated deformable porous media by the lattice Boltzmann method, *Transp. Porous Media* **99**, 427 (2013).
- [34] D. F. Boutt, B. K. Cook, B. J. O. L. McPherson, and J. R. Williams, Direct simulation of fluid-solid mechanics in porous media using the discrete element and lattice-Boltzmann methods, *J. Geophys. Res.* **112**, B10209 (2007).

- [35] I. Khan and C. K. Aidun, Direct numerical simulation of saturated deformable porous media using parallel hybrid lattice-Boltzmann and finite element method, *Int. J. Numer. Methods Eng.* **86**, 1379 (2011).
- [36] I. Khan and C. K. Aidun, Modeling the macroscopic behavior of saturated deformable porous media using direct numerical simulations, *Int. J. Multiphase Flow* **71**, 74 (2015).
- [37] I. Khan and C. K. Aidun, Investigating the effect of micro-structure on the deformation of saturated fibrous media using direct numerical simulations, *Comput. Fluids* **143**, 48 (2017).
- [38] L. Zhou, Z. G. Qu, L. Chen, and W. Q. Tao, Lattice Boltzmann simulation of gas-solid adsorption processes at pore scale level, *J. Comput. Phys.* **300**, 800 (2015).
- [39] L. Zhou, Z. G. Qu, T. Ding, and J. Y. Miao, Lattice Boltzmann simulation of the gas-solid adsorption process in reconstructed random porous media, *Phys. Rev. E* **93**, 043101 (2016).
- [40] H. Wang, Z. G. Qu, and L. Zhou, A combined GCMC and LBM simulation method for CH<sub>4</sub> capture in Cu-BTC particle adsorption bed, *Int. Commun. Heat Mass Transfer* **88**, 48 (2017).
- [41] Z.-Z. Li, T. Min, Q. Kang, Y.-L. He, and W.-Q. Tao, Investigation of methane adsorption and its effect on gas transport in shale matrix through microscale and mesoscale simulations, *Int. J. Heat Mass Transfer* **98**, 675 (2016).
- [42] S. Bakhshian, Z. Shi, M. Sahimi, T. T. Tsotsis, and K. Jessen, Image-based modeling of gas adsorption and deformation in porous media, *Sci. Rep.* **8**, 8249 (2018).
- [43] H. Wang, J. Q. Bai, Z. G. Qu, and M. Chang, Numerical study of heat transfer in process of gas adsorption in a Cu-benzene-1, 3, 5-tricarboxylic acid particle adsorption bed, *Int. J. Hydrogen Energy* **44**, 11989 (2019).
- [44] M. H. Chahbani, J. Labidi, and J. Paris, Effect of mass transfer kinetics on the performance of adsorbate heat pump systems, *Appl. Therm. Eng.* **22**, 23 (2002).
- [45] Q. Ma, Z. Chen, and H. Liu, Multiple-relaxation-time lattice Boltzmann simulation for flow, mass transfer, and adsorption in porous media, *Phys. Rev. E* **96**, 013313 (2017).
- [46] D. d'Humières, I. Ginzburg, M. Krafczyk, P. Lallemand, and L. Luo, Multiple-relaxation-time lattice Boltzmann models in three dimensions, *Philos. Trans. R. Soc., A* **360**, 437 (2002).
- [47] L. Chen, Y. Yu, J. Lu, and G. Hou., A comparative study of lattice Boltzmann methods using bounce-back schemes and immersed boundary ones for flow acoustic problems, *Int. J. Numer. Methods Fluids* **74**, 439 (2014).
- [48] W. Ren, C. Shu, and W. Yang, An efficient immersed boundary method for thermal flow problems with heat flux boundary conditions, *Int. J. Heat Mass Transfer* **64**, 694 (2013).
- [49] S. Tao, Q. He, J. Chen, B. Chen, G. Yang, and Z. Wu, A non-iterative immersed boundary-lattice Boltzmann method with boundary condition enforced for fluid-solid flows, *Appl. Math. Modell.* **76**, 362 (2019).
- [50] M. N. Linnick and H. F. Fasel, A high-order immersed interface method for simulating unsteady incompressible flows on irregular domains, *J. Comput. Phys.* **204**, 157 (2005).
- [51] S. Xu and Z. J. Wang, An immersed interface method for simulating the interaction of a fluid with moving boundaries, *J. Comput. Phys.* **216**, 454 (2006).
- [52] Y. Cheng and J. Li, Introducing unsteady non-uniform source terms into the lattice Boltzmann model, *Int. J. Numer. Methods Fluids* **56**, 629 (2008).
- [53] J. Wu, Y. Cheng, C. Zhang, and W. Diao, Three-dimensional simulation of balloon dynamics by the immersed boundary method coupled to the multiple-relaxation-time lattice Boltzmann method, *Commun. Comput. Phys.* **17**, 1271 (2015).
- [54] C. Zhang, Y. Cheng, L. Zhu, and J. Wu, Accuracy improvement of the immersed boundary-lattice Boltzmann coupling scheme by iterative force correction, *Comput. Fluids* **124**, 246 (2016).
- [55] Y. Cheng and H. Zhang, Immersed boundary method and lattice Boltzmann method coupled FSI simulation of mitral leaflet flow, *Comput. Fluids* **39**, 871 (2010).
- [56] L. Chen, G. Wu, E. F. Holby, P. Zelenay, W. Q. Tao, and Q. Kang, Lattice Boltzmann pore-scale investigation of coupled physical-electrochemical processes in C/Pt and non-precious metal cathode catalyst layers in proton exchange membrane fuel cells, *Electrochim. Acta* **158**, 175 (2015).
- [57] T. Zhang, B. Shi, Z. Guo, Z. Chai, and J. Lu, General bounce-back scheme for concentration boundary condition in the lattice-boltzmann method, *Phys. Rev. E* **85**, 016701 (2012).
- [58] X. D. Niu, C. Shu, Y. T. Chew, and Y. Peng, A momentum exchange-based immersed boundary-lattice Boltzmann method for simulating incompressible viscous flows, *Phys. Lett. A* **354**, 173 (2006).
- [59] Z. Z. Guo, C. G. Zheng, and B. C. Shi, Non-equilibrium extrapolation method for velocity and pressure boundary conditions in the lattice Boltzmann method, *Chin. Phys.* **11**, 366 (2002).
- [60] H. Z. Yuan, X. D. Niu, S. Shu, M. Li, and H. Yamaguchi, A momentum exchange-based immersed boundary-lattice Boltzmann method for simulating a flexible filament in an incompressible flow, *Comput Math. Appl.* **67**, 1039 (2014).
- [61] R. Machado, Numerical simulations of surface reaction in porous media with lattice Boltzmann, *Chem. Eng. Sci.* **69**, 628 (2012).